

DESICCATION RESISTANCE AND VISCOELASTICITY IN MODEL
MEMBRANE SYSTEMS

by

CHRISTOPHER WILLIAM HARLAND

A DISSERTATION

Presented to the Department of Physics
and the Graduate School of the University of Oregon
in partial fulfillment of the requirements
for the degree of
Doctor of Philosophy

June 2010

“Desiccation Resistance and Viscoelasticity in Model Membrane Systems,” a dissertation prepared by Christopher William Harland in partial fulfillment of the requirements for the Doctor of Philosophy degree in the Department of Physics. This dissertation has been approved and accepted by:

Dr. Daniel Steck, Chair of the Examining Committee

Date

Committee in charge: Dr. Daniel Steck, Chair
Dr. Raghuveer Parthasarathy, Research Advisor
Dr. Darren Johnson
Dr. Heiner Linke
Dr. John Toner

Accepted by:

Dean of the Graduate School

©June 2010

Christopher William Harland

An Abstract of the Dissertation of

Christopher William Harland for the degree of Doctor of Philosophy

in the Department of Physics to be taken June 2010

Title: DESICCATION RESISTANCE AND VISCOELASTICITY IN
MODEL MEMBRANE SYSTEMS

Approved:

Dr. Raghuveer Parthasarathy

Lipid membranes are a basic structural element of all cells. They provide a framework for the physical organization of the cell, act as a scaffold for numerous proteins, and serve as the host site for countless chemical reactions integral to cell function. Several key problems in membrane biophysics hinge on reliable methods for measuring membrane material properties. Properties such as rigidity, fluidity, charge density, etc., are important factors that govern membrane structure and function. As such, we need controllable, reliable, and quantitative methods of probing membrane material properties. In pursuit of such methods, we completed two related projects that, while distinct, aimed to create and apply quantitative measures of membrane material properties to current problems in biophysics.

The first of these two lines of inquiry centered on the pervasive, pathogenic family of mycobacteria that is known to not only cause several diseases but also to survive prolonged periods of dehydration. We developed an experimental model system that mimics the structure of the mycobacterial envelope consisting of an immobile hydrophobic layer supporting a two-dimensionally fluid, glycolipid-rich outer monolayer. With this system, we show that glycolipid containing monolayers, in great contrast to phospholipid monolayers, survive desiccation with no loss of integrity, as assessed by both fluidity and protein binding, revealing a possible cause of mycobacterial persistence.

In the second line of inquiry, we developed another general platform for probing membrane material properties that has produced the first reported observations of viscoelasticity in lipid membranes. We utilized recently developed microrheological techniques on freestanding lipid bilayer systems using high speed video particle tracking. The complex shear modulus of the bilayers was extracted at a variety of temperatures that span the liquid-ordered to disordered phase transition of the membranes. At many temperatures measured, the membranes displayed viscoelastic behavior reminiscent of a Maxwell material, namely elastic at high frequencies and viscous at low frequencies. Moreover, the viscoelastic behavior was suppressed at the critical phase transition temperature where the membranes behave as a purely viscous fluid. Surprisingly, the viscoelastic behavior was found in all of several distinct membrane compositions that were examined.

CURRICULUM VITAE

NAME OF AUTHOR: Christopher William Harland



GRADUATE AND UNDERGRADUATE SCHOOLS ATTENDED:

University of Oregon, Eugene, Oregon
University of Puget Sound, Tacoma, Washington

DEGREES AWARDED:

Doctor of Philosophy in Physics, 2010, University of Oregon
Master of Science in Physics, 2007, University of Oregon
Bachelor of Science in Physics, 2005, University of Puget Sound
Bachelor of Science in Mathematics, 2005, University of Puget Sound

AREAS OF SPECIAL INTEREST:

Membrane Biophysics, Biochemistry, Colloids, Cellular Biophysics

PROFESSIONAL EXPERIENCE:

Graduate Teaching Fellow, University of Oregon, 2005 – 2007

GRANTS, AWARDS AND HONORS:

NSF GK-12 Fellow, University of Oregon, 2007 – 2010

OCO Grant Competition (funding award for independent research in Janus colloids), University of Oregon, 2009 –2010

Seward Scholarship (awarded to the top undergraduate physics major),
University of Puget Sound, 2005

President's Scholarship (awarded for academic excellence), University
of Puget Sound, Tacoma, Washington, 2001 – 2005

Leonard Howarth Scholarship (awarded for academic excellence),
University of Puget Sound, Tacoma, Washington, 2001 – 2005

PUBLICATIONS:

Harland, C.W., Botyanszki, Z., Rabuka D., Bertozzi C.R.,
and Parthasarathy R.P. "Synthetic trehalose glycolipids confer
desiccation resistance to supported lipid monolayers" *Langmuir* **25**,
5193–5198, (2009).

Harland, C.W., Rabuka D., Bertozzi C.R., and Parthasarathy
R.P. "The *Mycobacterium tuberculosis* virulence factor trehalose
dimycolate imparts desiccation resistance to model mycobacterial
membranes" *Biophys. J.* **94(12)**, 4718–4724, (2008).

ACKNOWLEDGEMENTS

Thank you to my wife for countless practice talks heard and endless streams of wisdom about work, life, and the rest. I will be forever appreciative of my advisor, Raghu, for consistently being invested in my success as a scientist. Thank you to my family for their support and encouragement throughout my life. I would have been lost in graduate school without the companionship of Nate Kuwada and Mick Davis. Their friendship and advice were crucial components to my progress throughout the past five years.

TABLE OF CONTENTS

Chapter	Page
I. INTRODUCTION	1
II. LIPID MEMBRANES: FORMATION, IMAGING, AND ANALYSIS	5
Introduction	5
Lipid Membrane Formation	5
Supported Monolayers	6
Freestanding Lipid Bilayers	10
Microscopy and Imaging	14
Fluorescence Microscopy	15
Fluorescence Interference Contrast Microscopy	18
Membrane Statistical Mechanics	21
Brownian Motion and Diffusion	21
Fluorescence Recovery After Photobleaching	25
Particle Tracking and Analysis	28
III. LIPID DERIVED DESICCATION RESISTANCE	33
Introduction	33
Glycolipid Derived Desiccation Resistance	34
Desiccation Resistance in Model Mycobacterial Membranes	35
Model Mycobacterial Membranes	36
Measurement of Desiccation Resistance	40
Synthetic Trehalose Glycolipid Derived Desiccation Resistance	45
Measurement of Desiccation Resistance	46

Chapter	Page
Evidence Against a Percolation Model	51
Summary and Outlook.....	54
IV. VISCOELASTICITY IN LIPID BILAYERS.....	57
Introduction	57
Free-standing Lipid Bilayers	58
Membrane Material Properties	59
Lipid Membrane Phases	59
Viscoelasticity.....	60
Microrheology	61
Particle Tracking Microrheology	61
Controls and Tests	65
Viscoelasticity in Lipid Bilayers	71
Viscoelasticity.....	71
Temperature Sensitivity	73
Summary and Outlook.....	75
Two-Point Microrheology	76
APPENDIX: PERCOLATION SIMULATION	80
BIBLIOGRAPHY	82

LIST OF FIGURES

Figure	Page
1.1 Membrane Schematic	2
2.1 Langmuir-Blodgett Deposition	9
2.2 Freestanding Lipid Bilayer System	12
2.3 Freestanding Lipid Bilayer Substrates	13
2.4 Freestanding Lipid Bilayer Deposition	14
2.5 Freestanding Lipid Bilayer Example	15
2.6 Fluorescence Microscope	17
2.7 Fluorophore Spectra	18
2.8 FLIC Schematic	19
2.9 Random Walkers	24
2.10 FRAP Schematic	26
2.11 FRAP Data	27
2.12 Diffraction Limit	29
2.13 Airy Disk	30
2.14 Particle Tracking Accuracy	31
2.15 Particle Tracking Procedure	32
3.1 Model Mycobacterial Membrane Schematic	37
3.2 FLIC Measurement	38
3.3 AFM Measurement	39
3.4 TDM and DOPC Supported Monolayers	41
3.5 TDM Desiccation Recovery	43
3.6 Synthetic Trehalose Glycolipid Structures	47
3.7 Synthetic Trehalose Glycolipid Monolayers	48
3.8 Comparison Between TDM and Synthetic Trehalose Glycolipids	50
4.1 Maxwell Material	67
4.2 Frame Rate Dependence	68

Figure	Page
4.3 Microrheology of a Common Viscous Fluid	70
4.4 Microrheology of a Viscoelastic Fluid	70
4.5 DMPC/DOPC Complex Shear Moduli	72
4.6 Crossover Frequencies	74
4.7 Two-Point Microrheology	77
4.8 Simulated Two-Point Data	78
A.1 Triangular Site Percolation Lattice	81

CHAPTER I

INTRODUCTION

All living things are made of cells and a basic structural element of cells is the lipid membrane pictured in Figure 1.1. The ubiquitous presence of the lipid membrane and its importance in life as the interface between individual cells and their environment as well as between internal organelles and the cytoplasm places emphasis on understanding the structure, properties, and functions of this bio-material. While much is known about the biological function of lipid membranes and their chemical composition [1–3], little is known about how these compositions and functions determine or are determined by the material properties of the membrane itself. Determination of these material properties will allow for the understanding of the many far from equilibrium structures seen in nature.

The membrane is a remarkable two-dimensionally fluid surface that adapts and changes its composition, structure, and functions to carefully balance and facilitate interactions between the internal and external cellular environments. From a materials science standpoint, many of the lipid membrane's remarkable functions depend on and in part are explained by its underlying material properties, particularly that of self-assembly, fluidity, and rigidity. The self-assembly of lipid membranes is made possible by the amphipathic nature of individual lipid monomers. Lipids consist

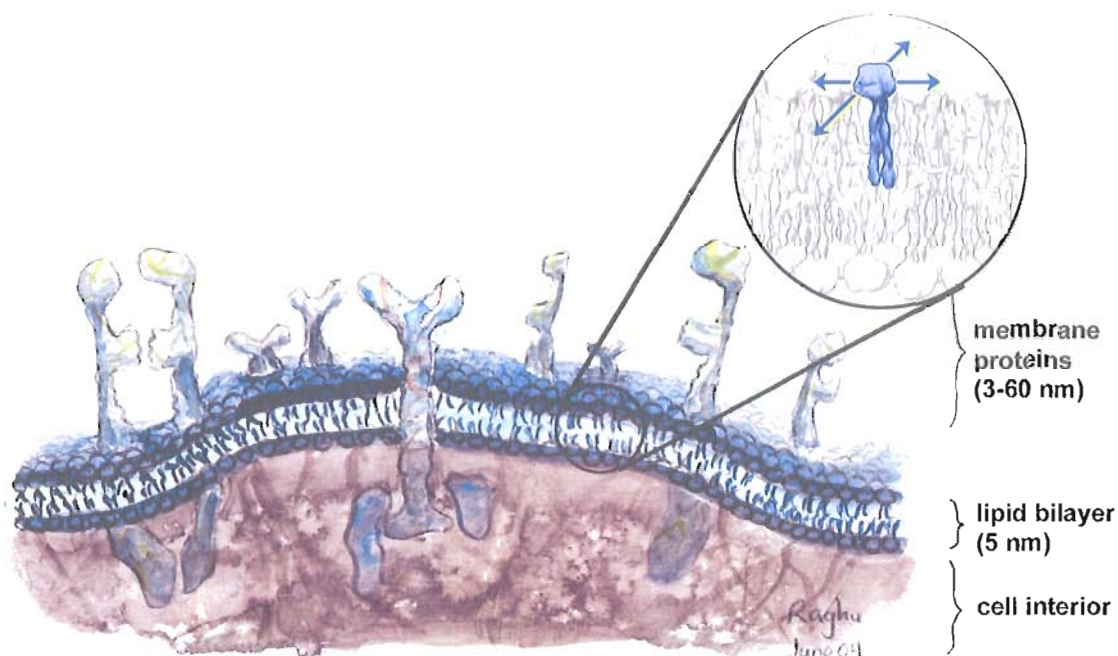


Figure 1.1: Lipid bilayer membrane schematic with an inset highlighting the self assembly of individual lipid monomers. The membrane itself is composed of a lipid bilayer and associated proteins. The interactions between individual lipids and proteins determine the overall membrane material properties. Illustration by Raghuveer Parthasarathy.

of a hydrophilic headgroup and a hydrophobic tailgroup. The formation of a lipid membrane occurs as an entropic consequence of the hydrophobic interactions between tailgroups and hydrophilic interactions between headgroups and a surrounding polar solvent. From this construction follows the natural fluidity of lipid membranes. Since membranes are held together with hydrophobic/hydrophilic interactions and not chemical bonds, lipid monomers are able to diffuse in the two-dimensional plane of the membrane. This dissertation focuses on this intrinsic property of membranes, fluidity, that serves as a measure of membrane integrity and stands as an important property to characterize and quantify.

The structure and formation of lipid membranes is discussed in Chapter II along with details of experimental procedures and common techniques employed in membrane work. Accompanying this is a primer on the statistical mechanics of a biological environment with emphasis placed on the information contained within thermally driven Brownian motion. The chapter concludes with a collection of examples that show how we can extract physical information from a biological system.

We begin the investigation of membrane material properties in Chapter III where we explore issues of membrane integrity and self-assembly. Specifically, we focus on the ability of certain lipids, originating from mycobacteria, to provide desiccation resistance to membranes of which they are constituents. An overview of relevant mycobacterial membrane chemistry is provided alongside information pertaining to the microbiological issues related to desiccation resistance. The chapter details our experimental monolayer mimic system and measurements of membrane integrity. We report the first observations of lipid derived desiccation resistance by both natural and synthetic glycolipids. Chapter III concludes with a discussion of future work involving other mycobacterial lipids and drug delivery technologies.

In Chapter IV we focus directly on membrane fluidity. Employing recent techniques involving high-speed video particle tracking, we measure the Brownian dynamics of small tracers attached to lipid membranes. From these measurements we extract complex shear moduli as a direct measure of fluidity. The viscoelastic fluid response of the membranes is characterized as a function of temperature and

compared to a simple mechanical analog model. The chapter includes details of a different lipid membrane geometry than is found in Chapter III as well as a lengthy discussion of extracting fluid properties from Brownian dynamics. We report the first observations of viscoelastic behavior in pure lipid bilayers. Chapter IV concludes with a discussion, and preliminary data, of future directions.

Both projects in this dissertation involved the development of new experimental platforms that are adaptable and support further investigations in continuing and new directions. The concluding sections of Chapters III and IV provide examples of future work that take advantage of the experimental platforms. While Chapter II serves as a general reference for membrane biophysicists, this dissertation as a whole provides all the tools necessary to perform new investigations pertaining to lipid membrane material properties and directly apply such characterizations to contemporary problems in not only membrane biology, but also soft condensed matter physics.

CHAPTER II

LIPID MEMBRANES: FORMATION, IMAGING, AND ANALYSIS

Introduction

In a biophysics lab, it is often useful to familiarize oneself with the entire process of sample creation, experimentation and data collection, analysis, and interpretation (often including computer modeling). Doing so is not only beneficial to completing research but also provides a wider understanding of the scientific process. This chapter provides an overview of laboratory techniques, devices, models, and interpretations that should be applicable to any membrane biophysics lab and will be useful to future students. Later chapters will reference methods found here.

Lipid Membrane Formation

In nature, self assembling processes are widespread and used to create mesoscopic structures from small monomer units. This phenomenon is highly efficient requiring effort only in creating and programming the monomer units while leaving the complex combination of these units into higher-order structures to the laws of physics. Lipid membranes are wonderful example of this process, see Figure 1.1. The membranes, composed of self-organized lipid monomers and proteins, are constructed

to take advantage of hydrophobic and hydrophilic interactions. Each individual lipid possesses a hydrophobic tail group with corresponding hydrophilic head group. These groups can vary from lipid to lipid but the amphiphilic construction of the lipid is conserved. The following phospholipids are used throughout the studies presented in this dissertation: 1,2-dioleoyl-*sn*-glycero-3-phosphocholine (DOPC), 1,2-dimyristoyl-*sn*-glycero-3-phosphocholine (DMPC), 1,2-dipalmitoyl-*sn*-glycero-3-phosphoethanolamine-N-(cap Biotinyl), 1,2-dimyristoyl-*sn*-glycero-3-phospho-L-serine (DMPS), 1,2-dilauroyl-*sn*-glycero-3-phosphate (DLPA), and 1,2-dinervonoyl-*sn*-glycero-3-phosphocholine (DNPC). These lipids were purchased from Avanti Polar Lipids (Alabaster, AL).

Creating synthetic lipid bilayers relies on the construction of a substrate or environment that will exploit the amphipathic lipids' construction. Supported lipid monolayers (detailed below) are created by hydrophobically treating a substrate with molecules similar to a lipid tail and forcing the lipid monomers to act as a surfactant between the given substrate and an aqueous environment. Similarly, the construction of a freestanding lipid bilayer hinges on the creating a hydrophobic chemical environment in the vacated spaces of an otherwise hydrophobic substrate. In the following sections the details of these membrane geometries will be presented.

Supported Monolayers

One of the most simple lipid membrane systems is the supported lipid monolayer [4, 5]. This system, in general, consists of a fluid lipid monolayer deposited on

a substrate, usually silicon, mica, glass, or quartz, that has been coated with an immobile, hydrophobic molecule like an alkane-silane or alkane-thiol. These immobile lower layers, after deposition, are often simple carbon chains of varying length (usually 10 - 22 carbons). The interaction between the lipid tail groups and these hydrophobic coating molecules provides an entropic incentive for the monolayer to bind to the substrate. These samples are quick to prepare, provide excellent compositional control, and conserve raw materials (both lipid and substrate). Most importantly, monolayers mimic the natural fluidity of cell membranes.

Our work in lipid derived desiccation resistance benefited greatly from the use of lipid monolayers in our model mycobacterial membrane system as detailed in Chapter III. The fabrication of such a system proceeded as follows: silicon/silicon oxide substrates were hydrophobically treated, lipid mixtures were prepared, finally mixtures were deposited via Langmuir-Blodgett deposition [4, 5]. The substrate coating began by cutting a large (10cm diameter) silicon wafer with a 54nm oxide layer into multiple 1cm squares followed by a piranha solution cleaning (3:1 concentrated sulfuric acid/30% hydrogen peroxide). These squares were then dried and incubated with 3mM octadecyltrichlorosilane (OTS), purchased from Sigma-Aldrich, in toluene for 3 hours. OTS chemically binds to the SiO_2 surface. After incubation, the wafers were rinsed with clean toluene, dried, and placed in an oven for at least 4 hours at 100 °C which cross-links the silane groups [6]. The baked wafers were then rinsed again with clean toluene and ethanol (use of strong cleaning agents removes the OTS

monolayer) and the hydrophobicity of the OTS coating was assessed by dropping $10\mu\text{l}$ of ultrapure water on the chip and observing a near 90° contact angle as measured relative to the wafer surface.

These OTS treated wafers served as our hydrophobic substrates. The lipid mixtures deposited on these substrates were first mixed in chloroform to the proper molar ratios. A typical monolayer would consist of 0.5 to 3.0 mol% fluorescent lipid, using larger amounts of fluorescent lipid leads to self quenching and no fluorescence is observed. Common fluorescent lipids are: Texas Red 1,2-dihexadecanoyl-*sn*-glycero-3-phosphoethanolamine (TR-DHPE, purchased from Invitrogen) and 1-acyl-2-nitrobenzofuran-*sn*-glycero-3-phosphocholine (NBD-PC, purchased from Avanti Polar Lipids). If a biotinylated lipid was used about 3.0 mol% of the overall composition is 16:0-Biotinyl-CAP-PE (Avanti Polar Lipids). The remaining content of the lipid composition was experiment-dependent. For the glycolipid dehydration resistance experiments the composition was 99-X:X trehalose glycolipid:DOPC where the fraction of DOPC, X, was varied from 0 to 0.99. All lipids were prepared and stored in chloroform.

A lipid monolayer of the desired composition was formed at an air/water interface and transferred to hydrophobically treated substrates via Langmuir-Blodgett deposition [7, 8], see Figure 2.1. Samples were deposited in a small two- or eight-well chamber containing $400\mu\text{l}$ (eight-well) or 4ml (two-well) of water or phosphate buffered saline (PBS). Lipid mixtures in chloroform were injected onto the water/PBS

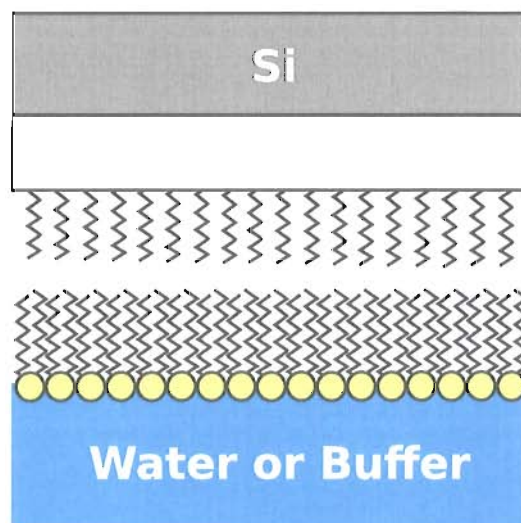


Figure 2.1: Schematic illustration of a Langmuir-Blodgett deposition. A lipid monolayer (yellow circles) is formed at the air/water or buffer interface leaving the hydrophobic tails exposed with the hydrophilic headgroups buried in the aqueous subphase. To form the supported monolayer a alkane-silane coated silicon/silicon oxide substrate is lowered into the exposed monolayer. Hydrophobic and hydrophilic interactions hold the lipid monolayer to the substrate as it is submerged into the aqueous subphase.

surface in the chambers in 5 to 10 μ l increments with a microsyringe, forming a lipid monolayer at the air/fluid interface. The surface tension of the water/PBS/lipid mixture was monitored with a Kibron tensiometer. The tensiometer was first calibrated and zeroed to the known surface tension of water (72.8mN/m). As lipid was deposited on the surface the tension decreased indicating the formation of an ordered monolayer at the air/water interface. Lipid was added until maximum surface packing was reached (about 30mN/m for most lipids) and further addition of lipid did not influence the surface tension. Adding lipid beyond the maximally packed amount resulted in excess lipid forming micelles and falling out of solution to the bottom of the chamber, this could be seen with the naked eye.

Once the desired surface tension value had been reached, the tensiometer was withdrawn and the aforementioned hydrophobically treated silicon/silicon oxide wafers were lowered into the lipid monolayer at the air/water interface as shown in Figure 2.1, a process known as Langmuir-Blodgett deposition. The deposition proceeded by lowering the hydrophobically treated substrate from the air, through the lipid monolayer, and into the water/PBS with the hydrophobically treated side facing down into the lipid monolayer. The deposition proceeded at 6mm/min. Once the wafer completely broke the surface and was submerged sufficiently (no fluid meniscus present), the wafer was released from its holder. The entire chamber was then submerged in a larger beaker of water/PBS to dilute and remove unbound lipid from the sample and chamber. It was often useful to transfer the wafer, now with bound monolayer, to another well in the chamber to avoid interference from unbound lipid in the deposition chamber. After successful deposition, monolayers were stable for 1 to 3 days if left in the fluid chamber and were surprisingly resilient while being moved and transferred from chamber to chamber as long as all movement/transfers take place while submerged.

Freestanding Lipid Bilayers

While supported monolayers are a quick, robust, and versatile model membrane system, they differ from cell membranes by being in contact with a supporting substrate. It has been shown that substrates influence membrane fluidity and diffusion in supported monolayers and bilayers [9–11]. The most obvious way to see the

influence is to simply measure the diffusion coefficient of a supported monolayer and notice its difference from that observed in vesicles, cell membranes, or freestanding lipid bilayers. The goal of studies of membrane fluidity is to measure this property in the absence of substrate influence. As such, we work with a support free system known as freestanding lipid bilayers, see Figure 2.2. Freestanding lipid bilayers are widely used to investigate the biophysics of channel proteins[12, 13], membrane permeation [14], and support free lipid dynamics and organization [15–17].

We used gold-coated transmission electron microscope (TEM) grids as our freestanding lipid bilayer substrates. The TEM grids were purchased from SPI in both 100 and 200 hex varieties, see Figure 2.3. The 100 hex grids were 1mm in diameter with 100 holes at $215\mu\text{m}$ wide each. The 200 hex grids were also 1mm in diameter with 200 holes at $100\mu\text{m}$ wide. We incubated the TEM grids with 0.6M octadecylthiol (ODT), purchased from Sigma-Aldrich, in ethanol or methanol for at least 4 hours. The thiol groups bind to the gold coating of the TEM grids. After incubation, the coated grids were washed with clean ethanol and dried with a stream of nitrogen [18, 19].

Deposition of a freestanding lipid bilayer (Figure 2.4) proceeded via a vertical Langmuir-Schaefer deposition [20–24]. Briefly, desired lipid compositions were mixed in chloroform (often with the inclusion of biotinylated lipids) and this mixture was injected onto 4ml of water/PBS in a small chamber. The surface tension was again monitored and lipid was added until maximal surface packing was attained

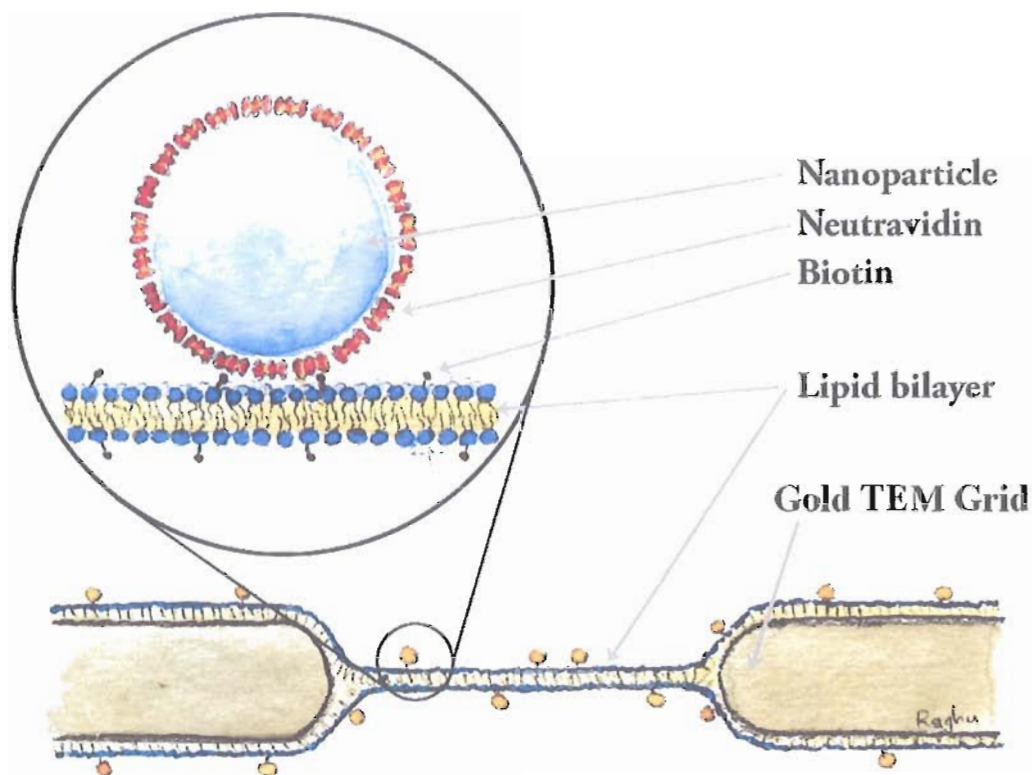


Figure 2.2: Side-on drawing of the freestanding lipid bilayer system used in microrheological measurements. The substrate, a gold TEM grid, is hydrophobically treated and a lipid monolayer is deposited on both sides of the grid simultaneously. At regions in the substrate where holes appear, the two monolayers come together to form a bilayer. The inset shows a magnified view of the freestanding lipid bilayer highlighting the bound fluorescent nanospheres used in particle tracking. Illustration by Raghuveer Parthasarathy.

(again around 30mN/m). To aid in the formation of freestanding lipid bilayers, the hydrophobically treated TEM grids were covered with $2\mu\text{l}$ of 3 to 40% squalene in hexane on each side. Squalene, an oil originally found in shark liver as well as many plants [25–27], went into the holes in the TEM grid and was left when the hexane quickly evaporated. The dried substrates then had a small amount of squalene in each hole that provided a highly hydrophobic region and favorable interaction for the

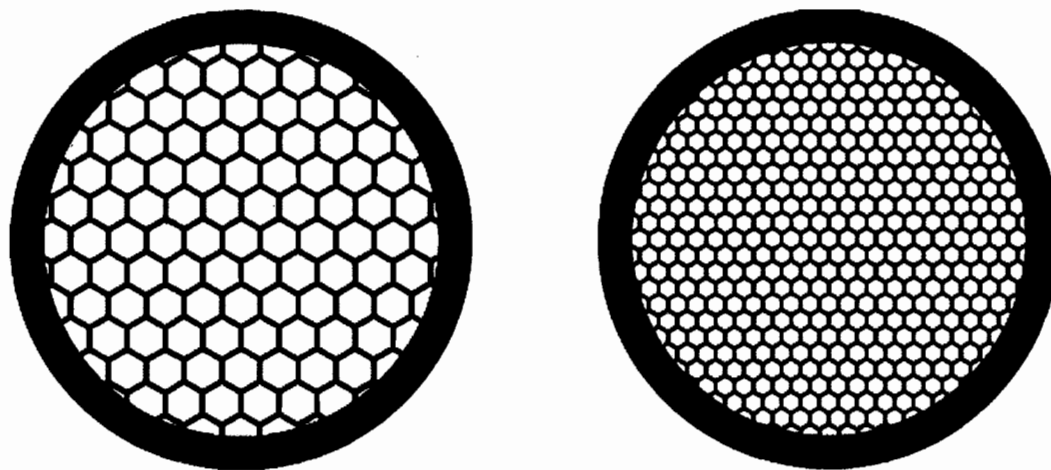


Figure 2.3: Transmission electron microscope used as freestanding lipid bilayer substrates. (*Left*) 100 hex grid with $215\mu\text{m}$ diameter holes. (*Right*) 200 hex grid with $100\mu\text{m}$ diameter holes. These gold coated substrates allow the deposition of freestanding lipid bilayers and the hole areas represent the regions that are free of substrate influence.

lipid tail groups encouraging bilayer formation. The TEM grid was then lowered, vertically, at $1\text{mm}/\text{min}$ into the lipid monolayer at the air/water interface. The vertical impingement of the TEM grid on the monolayer folded the monolayer up on both sides of the grid creating a separate monolayer on each side. The areas of the substrate with holes provided an opportunity for the monolayers to come together with the help of the squalene.

After the TEM grid was entirely submerged, the chamber was placed in a larger beaker of water/PBS and the substrate was transferred to a new chamber. This transfer often causes freestanding lipid bilayers to rupture so much care is needed to keep the grid parallel to the direction of motion at all times in order to minimize the lateral pressures on the freestanding lipid bilayers. The grid was then allowed

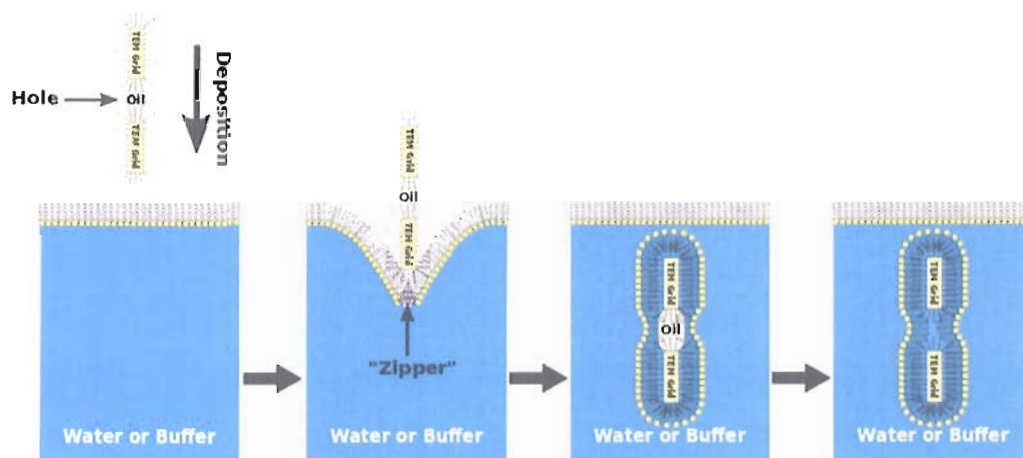


Figure 2.4: Schematic of freestanding lipid bilayer deposition. (*Left*) the hydrophobically treated gold TEM grid is lowered vertically into the lipid monolayer at the air/water interface. (*Center*) as the substrate impinges on the surface the monolayer folds up on each side of the grid in a "zipper" motion. (*Right*) once submerged, the grid is coated with a lipid monolayer and in the hole regions of the substrate the two monolayers come together to form a bilayer. The oil trapped between the monolayers diffuses out over a few hours.

to equilibrate overnight to ensure that excess squalene trapped between layers of the freestanding lipid bilayers had diffused out into solution [21, 24]. Successfully deposited freestanding lipid bilayers containing fluorescent lipids can be seen in Figure 2.5.

Microscopy and Imaging

In the past two decades, the field of light microscopy has been host to a number of technical advances that allow for accurate, precise, and targeted images of biological samples to be gathered with relative ease. These advances are, in part, responsible for the recent explosion of high impact biophysical experiments. The ability to not

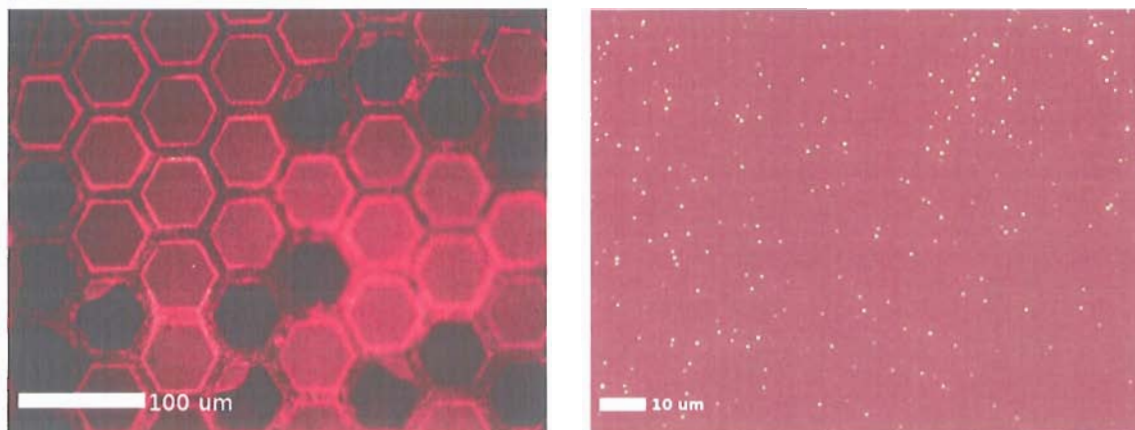


Figure 2.5: Freestanding lipid bilayer example. (*Left*) fluorescence image of a set of freestanding lipid bilayers deposited on a hexagonal TEM grid. Hexagons colored in uniform red represent freestanding lipid bilayers spanning the hole in the substrate whereas black hexagons are bilayer free holes. (*Right*) fluorescence image of 200nm nanoparticles (green) bound to a freestanding lipid bilayer (red). The small tracers' trajectories provide information about the material properties of the bilayer to which they are connected.

only take a detailed picture of a biological system but also take a series of high speed images of fluorescent markers attached to a sub-components of that system yield a large amount of dynamic information simply not accessible just a decade or two before. Along with the added utility provided by modern microscopy we are challenged to be sure that we draw the correct conclusions from our images. In this section we detail our imaging systems and in the following section address questions related to the interpretation of images taken by these systems.

Fluorescence Microscopy

Fluorescence microscopy provides a precise picture of our membrane systems. Moreover, our monolayers and bilayers are 3 to 5nm thick and scatter very little light requiring the presence of fluorescent lipids and probes for imaging. A typical inverted

fluorescence microscope, Figure 2.6, consists of the usual microscope body including stage, eye piece, objective lens and condenser lamp and adds an excitation light source and corresponding optical filters to separate excitation and emission light.

The basic principle of fluorescence centers on the illumination of a molecule that absorbs a particular wavelength of light and emits light at a longer wavelength (Figure 2.7). The separation of these two processes, aided by optical filters, allows us to image our samples with low background and great specificity. Low background is the result of filtering out all light outside of our emission bandwidth while the specificity is derived from directed labeling of interesting sample components with fluorescent molecules. Fluorophores are commercially available in a wide range of excitation/emission combinations and specific binding agents. We commonly use Texas Red and NBD fluorophores, Figure 2.7, in our samples as they are spectrally distinct, widely available, and well characterized.

As an excitation source we use a 100W mercury arc lamp since its spectrum covers a broad range of fluorophores. In our particular experiments, we utilized a Nikon TE-2000 inverted fluorescence microscope equipped with the aforementioned mercury arc lamp. High speed images, taken in Chapter IV, were acquired with a complementary metal-oxide-semiconductor camera (PCO.1200s; PCO AG) using CAMWARE software and membrane images, in both Chapter III and IV, were taken with a more sensitive charge-coupled device camera (ORCA-ER; Hamamatsu) using

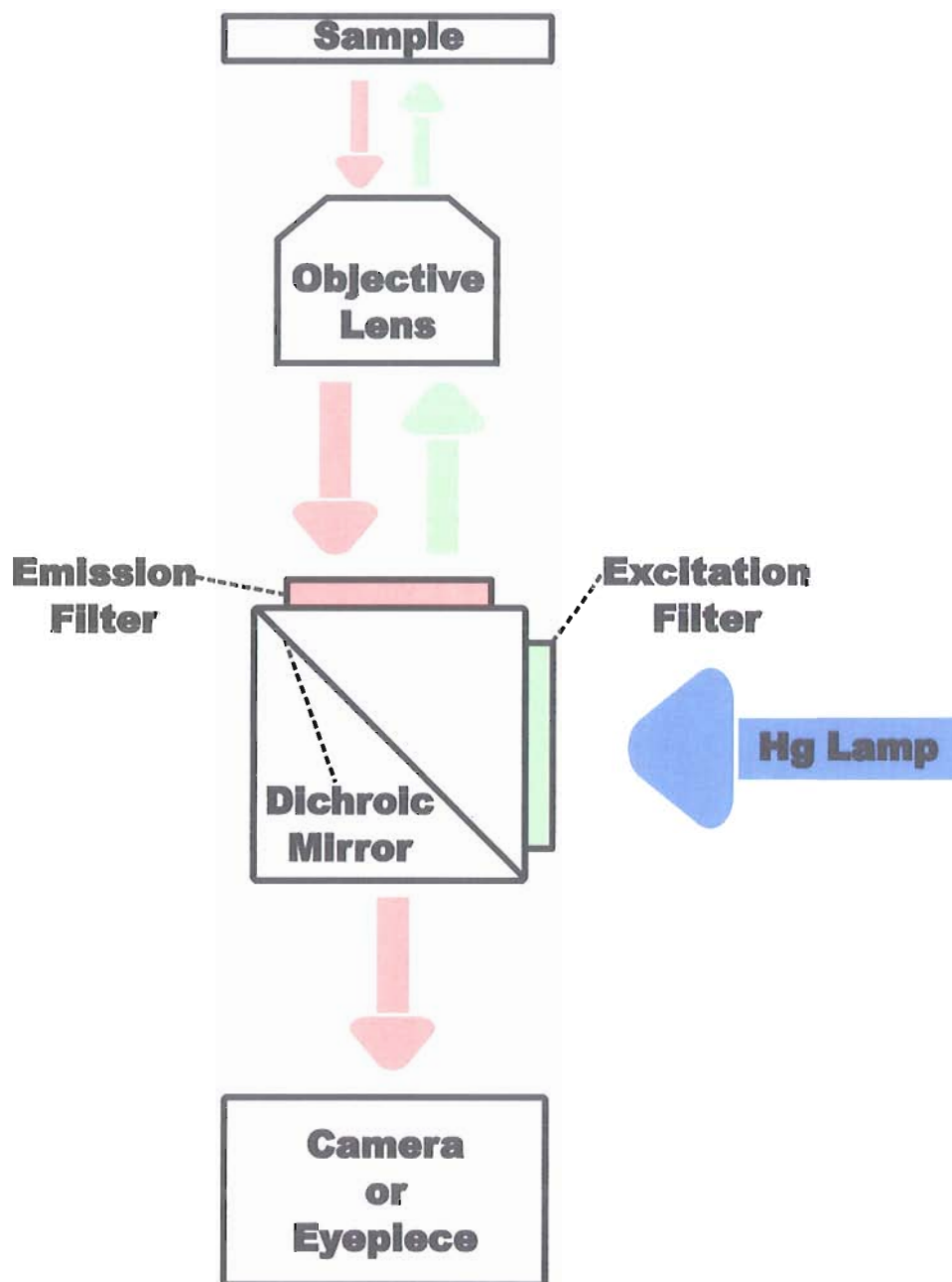


Figure 2.6: Schematic view of a typical inverted fluorescence microscope (not to scale). The inverted objective lens allows for imaging without immersion into the aqueous environment that usually accompanies biological samples. The mercury lamp excitation source, coupled with the filter system, allow for the use of multiple fluorophores and selective imaging of each channel.

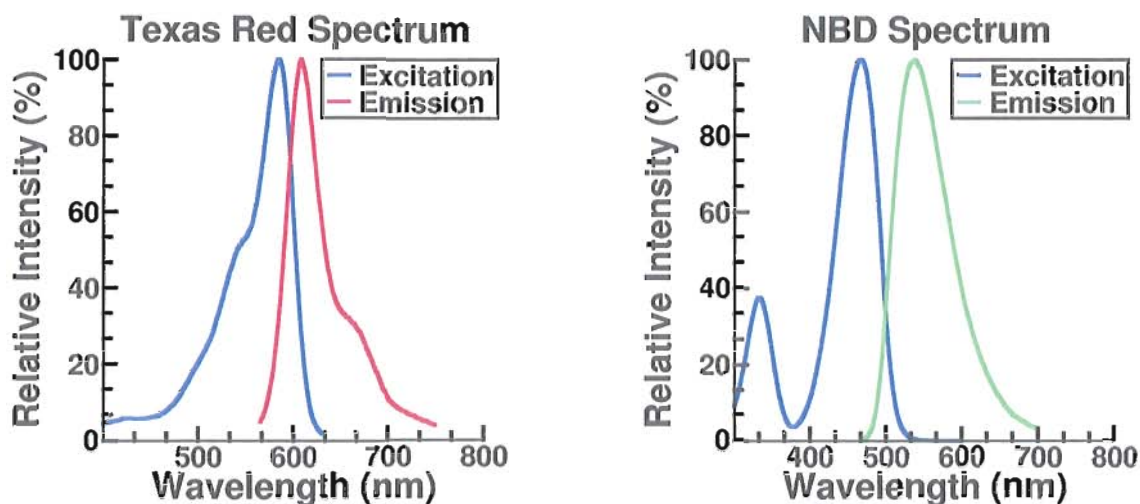


Figure 2.7: Common fluorophore spectra. (*Left*) spectrum of Texas Red with peak excitation and emission at 589nm and 615nm, respectively. (*Right*) spectrum of NBD with peak excitation and emission at 466nm and 539nm, respectively. In a fluorescence microscope, a dichroic or polychroic filter is used that reflects all excitation light and allows all emission light to transmit. This filter coupled with narrow (20nm width) bandpass filters at the light source and detection camera allow for the precise excitation and observation of fluorophores.

Nikon Elements software. Images were taken at a variety of magnifications using Nikon 10x, 20x, 60x (NA = 0.9), and 60x oil immersion lenses.

Fluorescence Interference Contrast Microscopy

The use of fluorescence as opposed to conventional bright field microscopy provides additional benefits beyond color labeling, selectivity, and low background. One such advantage is the ability to use the interference of fluorophore emission light to infer the height of the fluorophore above a reflective substrate. This method, known as FLIC, uses the isotropic emission of light from a fluorophore to relate the interference pattern that results when the fluorophore is near a reflective surface to the distance of the fluorophore from the reflective surface [28]. As shown in Figure 2.8, lipid bound

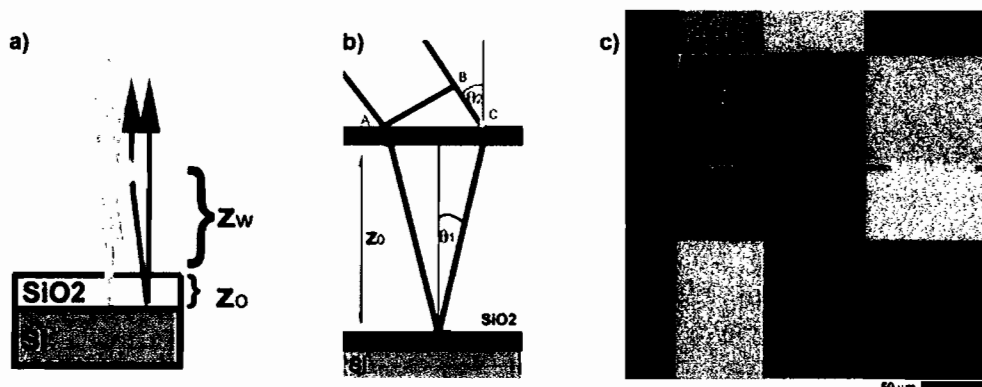


Figure 2.8: Fluorescence interference contrast microscopy (FLIC) schematic. **a)** Diagram of two representative excitation and emission rays from a fluorophore near a reflective substrate. **b)** Detailed view of the optical geometry involved in calculating the interference of fluorophore emission light that travels directly to the detector and light that reflects from the substrate before traveling to the detector. **c)** Fluorescence image of a typical FLIC measurement on a support monolayer. The 16 different shades of gray represent 16 different oxide layer thicknesses (optical path lengths). This image provides 16 measures of interference intensity as a function of the known oxide thicknesses. Image adapted from [28].

fluorophores absorb and emit light isotropically. Simultaneously emitted light can travel directly to a detector or reflect from a supporting substrate and then travel to the detector. These two light rays have different path lengths representing the different distances traveled and like all coherent light rays of differing path lengths will interfere with each other at the detector producing an interference pattern.

The interference pattern contains information about the path length difference. The physical situation is somewhat more complicated than the simple example stated above since there are more than two possible paths for the light to take to the detector but nonetheless, the principle holds. As described in [28], it is straightforward to consider isotropic absorption and emission from a fluorophore near a reflective

substrate and integrate the intensity at a detector of all possible paths an emitted photon may take. The resulting intensity function takes the following form:

$$I_{FLIC}(z_o) = \sin^2 \left(\frac{2\pi}{\lambda_{ex}} (n_o z_o + n_w z_w) \right) \sin^2 \left(\frac{2\pi}{\lambda_{em}} (n_o z_o + n_w z_w) \right) \quad (2.1)$$

where n_o is the index of refraction in the transparent oxide layer, n_w is the index of refraction of the aqueous medium, λ_{ex} is the fluorophore excitation wavelength, λ_{em} is the fluorophore emission wavelength, z_o is the oxide layer height, and z_w is the height of the fluorophore above the oxide layer. Notice in Equation 2.1, that the excitation and emission wavelengths are dictated by the fluorophore in use and the index of refraction of the supporting substrate is known as is the index of the surrounding bulk medium. Therefore, if we were able to measure or design a substrate of varying transparent heights, z_o , we could then image the intensity as a function of these heights and use Equation 2.1 to calculate the fluorophore height above the substrate, z_w . We indeed make use of Si/SiO₂ substrates with 16 different levels of oxide thickness that were independently measured by depth profiler. It is then a simple task to image the different intensities of fluorophores on these chips, see Figure 2.8, and extract z_w as a fit parameter. We implement the intensity analysis and data fitting in MATLAB by generating a range of $I(z_o)$ curves for varying values of z_w and with λ_{ex} , λ_{em} , n_o , and n_w as experimentally constrained values. We then perform a least squares fit of these generated curves to the actual intensity curves as a function of oxide height, z_o . The best fit curve then reports the best fit height z_w .

Membrane Statistical Mechanics

As materials biophysicists, our approach to measuring membrane material properties often hinges on connecting a statistically varying observable to a physical force or material constant. Understanding the mathematical link between these observables and their corresponding physical counterparts is an essential component of our work. It is often desirable to characterize our membranes by measuring forces or material constants yet our imaging systems return only position and intensity (sometimes as a function of time). Therefore, our mathematical interpretations are the only bridge we have to connect what we see with what we desire to know. The following sections detail the connection between our observed quantities and physical properties. We begin with diffusion as it is a fundamental process in lipid membranes. We then detail two methods of measuring diffusion with many- and single-particle tracers.

Brownian Motion and Diffusion

Particles constantly undergo random thermal motion. This constant jiggling, referred to as Brownian motion in honor of Robert Brown [29, 30], plays a role in the spread of chemicals in your body and the motion of small particles in drops of water among other processes. While the term "random motion" implies images of complete chaos with no hope of extracting meaningful information, Brownian motion can in fact be well characterized in a manner that focuses on the statistical consistency of these systems and allows for the extraction of the system's material properties.

To appreciate the subtlety of a statistical characterization of Brownian motion it is useful to consider a non-random process first and subsequently compare it to the complimentary random process as Berg does in [31]. A person walking from one side of a room to the opposite side in a straight line is a well determined motion. The distance he/she travels from one side to the next, x , will be a function of the time, t , he/she spends walking and the number of steps they take, N . The relationship between the distance and time or step number is linear making this scenario quite simple:

$$x \propto Nt. \tag{2.2}$$

If we repeated this scenario many times the process and the outcome would be identical every time. The person would walk the same straight line, at the same speed, leaving from and arriving at the same points each time. Brownian motion is quite different and most noticeably so in the measurement of distance traveled as well as the path taken. The complimentary random process to our linear walker is unsurprisingly the random walker (a.k.a drunken sailor) who rather than taking one linear step after another to reach his/her destination instead randomly chooses between a forward or backward step. The random choice of forward or back is equally weighted. Now that we are considering each step as a random event it is useful to define a step size, δ , that is also present in the linear walker's sojourn but was not explicitly written down. Additionally, let us define the time it takes a random-walker to take a step as τ . Our question then is as follows: given a step size δ and a step

time τ , after total time t where does our drunken walk end up? Given the same information for our linear walker the answer was simple, the walker will end up on the other side of the room in a manner described in Equation 2.2. For the random walker the answer is also simple, we simply do not know where they will end up.

This does not mean that we cannot conclude anything about the random walker's motion. It simply means we cannot predict his/her position at a given time and must turn to statistical characterizations of his/her motion. While the motion of a single random walker is quite unpredictable, if we instead consider many random walkers we can talk about the average result of their motions. If we consider the average distance our random walker might travel we come to the uninteresting result of zero. The random walker is equally likely to go forward and backward during each step resulting in no net movement on average, $\langle x \rangle = 0$ where $\langle \rangle$ denotes the average for multiple random walkers. While the most likely traveled distance for such a walker is zero, in a sampling of a large number of random walkers many of them will travel a finite distance. We can simulate a random walk quite easily, note the analytical treatment below, and doing so for a large number of walkers allows us to construct a distribution of final distances, $\langle x \rangle$, that can be seen in Figure 2.9. This distribution is Gaussian, centered at zero, and its width determines the distance traveled in a typical random walk.

While the average distance traveled is zero, the random walkers are traveling and the longer they stumble around the more likely they are to cover some finite distance.

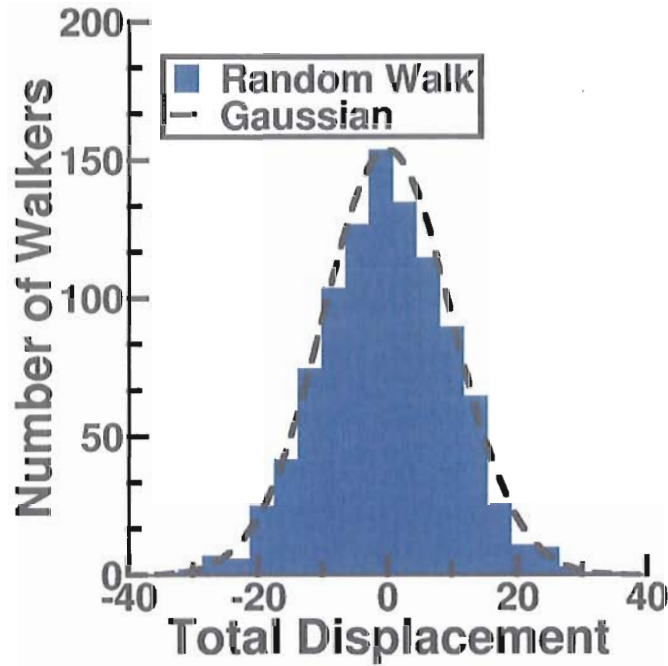


Figure 2.9: Average total displacement of 1000 random walkers and the corresponding Gaussian fit. As random walkers continue to walk they have a greater chance of a non-zero average displacement. The width of the distribution above provides information regarding the typical distance a random walker traverses.

We can see this when we consider the mean distance traveled squared, $\langle x^2 \rangle$. It is useful to measure the distance traveled as a function of the number of steps taken and we know $x(N) = x(N-1) \pm \delta$. We can then quickly calculate the mean squared displacement of the random walkers

$$\langle x^2(N) \rangle = N\delta^2 \quad (2.3)$$

where the cross term when squaring the mean squared displacement disappears since $\langle x(N) \rangle = 0$. To figure out how far the typical random walker travels we need only consider $\langle x^2(N) \rangle^{1/2} = N^{1/2}\delta$. Again recall that each step takes time τ which allows us to relate the total travel time to the number of steps, $N = t/\tau$. We can now relate

the typical distance traveled to the total time spent walking

$$\langle x^2(t) \rangle = \frac{\delta^2}{\tau} t = 2Dt \quad (2.4)$$

where $D \equiv \frac{\delta^2}{2\tau}$ is the definition of the one-dimensional diffusion coefficient of a random walker. We can now see that a random walker has a well defined typical travel distance that is proportional to the square root of the time spent walking. The constant of proportionality, D , and the power of time in Equation 2.4 are both factors that contain information of the type of traveling experienced by the random walker. As we will see in Chapter IV, the material properties of a given system heavily influence these factors and in the following sections details on how to measure such factors will be presented.

Fluorescence Recovery After Photobleaching

A commonly used method for measuring diffusion in lipid membranes is fluorescence recovery after photobleaching (FRAP), depicted in Figure 2.10, which measures diffusion of many lipids in a small area of the membrane. The principle of FRAP centers on the diffusion of individual lipids and the irreversible bleaching of lipid bound fluorophores. Molecular fluorophores, after absorbing excitation light, can either decay by emitting a lower energy photon or by a non-radiative pathway that may involve the breaking or reconfiguring of chemical bonds. If the fluorophores decay via a non-radiative pathway the breaking of chemical bonds irreversibly ceases fluorescence, resulting in so called bleaching. These fluorophores go dark and have no ability to begin fluorescing again but they are still free to diffuse within the membrane.

Exploiting fluorophore bleaching to measure diffusion is achieved by bleaching a small, circular region of lipids within a membrane. The dark lipids continue to undergo normal diffusion as do the fluorescing unbleached lipids. As the bleached lipids diffuse away from the spot and the fluorescing lipids diffuse into the spot the mean intensity in the bleached region increases. After a time, dependent on the lipid diffusion coefficient, there will be no evidence of the bleached spot and membrane fluorescence intensity will be homogeneous.

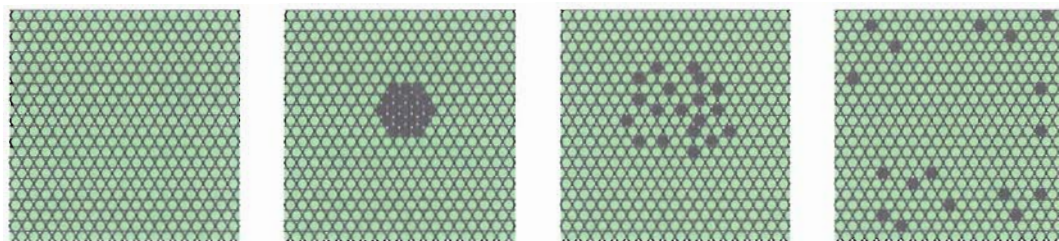


Figure 2.10: Representative FRAP schematic diagram. (*Left*) triangular lattice of fluorescing lipids (green). (*Center, left*) irreversibly bleached selection of lipids (black). (*Center, right*) some time later, diffusion of bleached lipids away from the center spot and diffusion of unbleached lipids into the previously bleached area. (*Right*) long time result of bleached and unbleached lipid diffusion recovers uniform fluorescence with a lower overall intensity and no evidence of a center spot.

The general experimental procedure is as follows: use an aperture, laser, or high magnification objective to focus fluorescence excitation light to a small spot on a lipid membrane, increase the intensity of the excitation light to bleach the majority of the fluorophores in the spot (typically 10 to 20s), take 3 to 6 images as the dark spot recovers uniform fluorescence (typically 60 to 100s), see Figure 2.11. The common approach to analyzing FRAP data includes many more images and fitting the intensity recovery of the spot to an analytical function [32]. While this is effective, we employ a

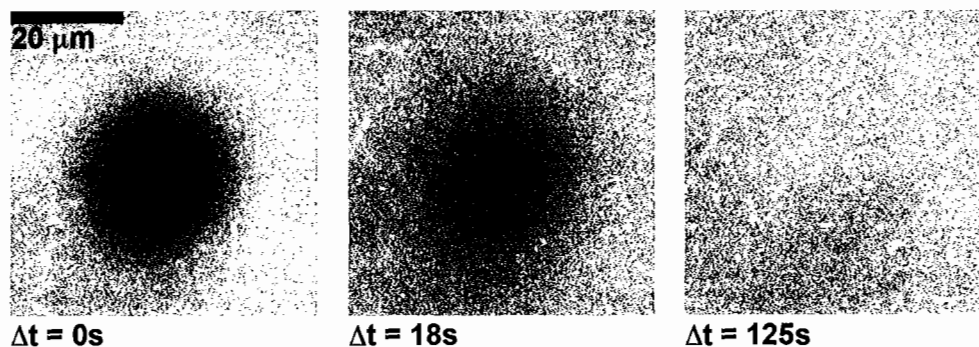


Figure 2.11: Example of FRAP data for a typical supported lipid monolayer. (*Left*) a small circular area of fluorescent lipids is bleached by exposing lipids in this area to high intensity mercury arc lamp light shaped by a small aperture. (*Middle*) after a small amount of time the permanently bleached lipids have diffused away from the spot while unbleached lipids diffused into the spot. (*Right*) about 2 minutes after the initial bleaching we recover homogeneous fluorescence intensity in the entire field of view. The overall intensity of the area has been reduced due to the bleached fluorophores but no evidence of a spot exists.

method that uses only 3 or 4 images and exploits the fundamental principle of FRAP, the diffusion of unbleached and bleached lipids [33]. Rather than fit the intensity recovery, we take the initial image of the bleached spot and successively blur the image by simulating the diffusion of the pixels in the image. A range of diffusion coefficients are chosen and random pixel diffusion is carried out on the initial spot image. The simulated images are then compared to the subsequent real membrane images and the diffusion coefficient that most accurately produces the actually blurring observed in the membrane is chosen as the bulk coefficient.

Particle Tracking and Analysis

Particle tracking is a useful and well utilized method of collecting position information over time for small micro and nanoparticles. This method provides an accurate and precise method for characterizing the Brownian motion present in many systems including lipid membranes. In general, the process involves imaging particles in fluorescence or bright field, preferably at high frame rates, processing those images to isolate the particles, and fitting their intensity distribution to determine their centroid.

By fitting a 2D Gaussian to the particle images we obtain sub-pixel tracking accuracy. On the first tracking pass particle locations are determined by simply finding the brightest local pixel. This method limits our accuracy to the resolution of our microscope, objective lens, and camera combination (typically about 110nm per pixel). However, by using a 2D Gaussian fit to the intensity gradient in the neighborhood of the local maxima, we can use the center of the analytical Gaussian function as the particle center.

The physical principles that allow for such a precise tracking are the same principles that prevent us from imaging the particle more accurately in the first place. The fluorescence of our probe molecules are subject to the diffraction limit that dictates the minimum size our fluorophores appear in the microscope is about $\frac{\lambda}{2}$. So instead of seeing a small, few nanometer, dot for each fluorophore we observe a diffuse spot typically 200 - 300nm in width shown in Figure 2.12. However, since our

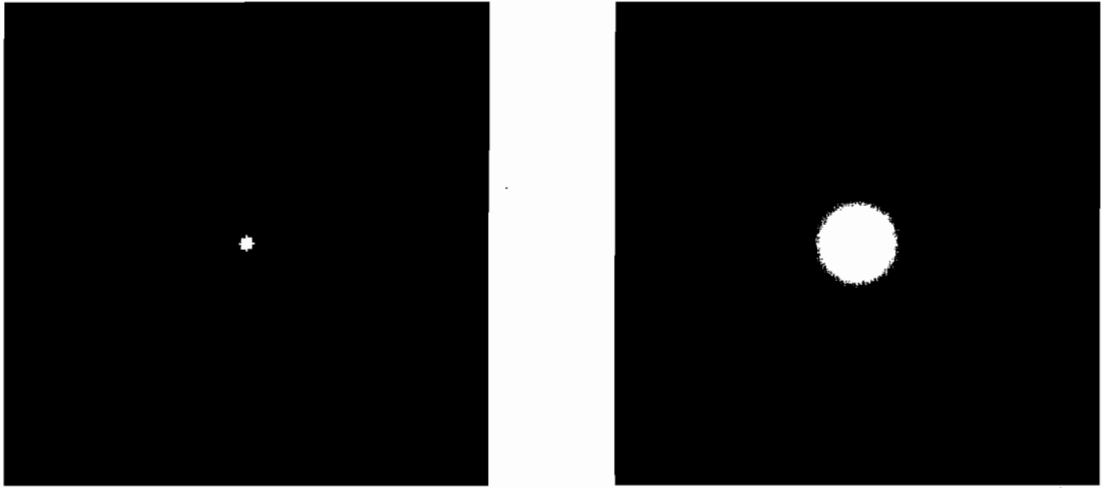


Figure 2.12: Example of the diffraction limit. (*Left*) representative image of a small particle or in this case a circular aperture with a diameter smaller than the wavelength of light diffracting from it. (*Right*) the Airy disk resulting from far field diffraction from this aperture. The disk is much larger and less detailed than the source but nonetheless the two share a common center. This center can be discerned by fitting an analytical 2D Gaussian to the diffuse spot.

fluorescing particles are spheres, the size and shape of our diffraction limited spot is given by the Airy function for far field Fraunhofer diffraction from a circular aperture [34]:

$$I(x) = I_0 \left(\frac{2J_1(x)}{x} \right)^2 \quad (2.5)$$

where the equation shown is for one-dimensional diffraction and $J_1(x)$ is the Bessel function of the first kind. The central peak of the Airy function is fit well by a simple Gaussian with width, σ , and center, x_0 , see Figure 2.13. Therefore, fitting a Gaussian to our particle images and extracting x_0 as our center provides location determination with an accuracy of $\pm \frac{\sigma}{2}$. Determining σ is done experimentally by drying particles on a glass slide such that they are completely immobile.

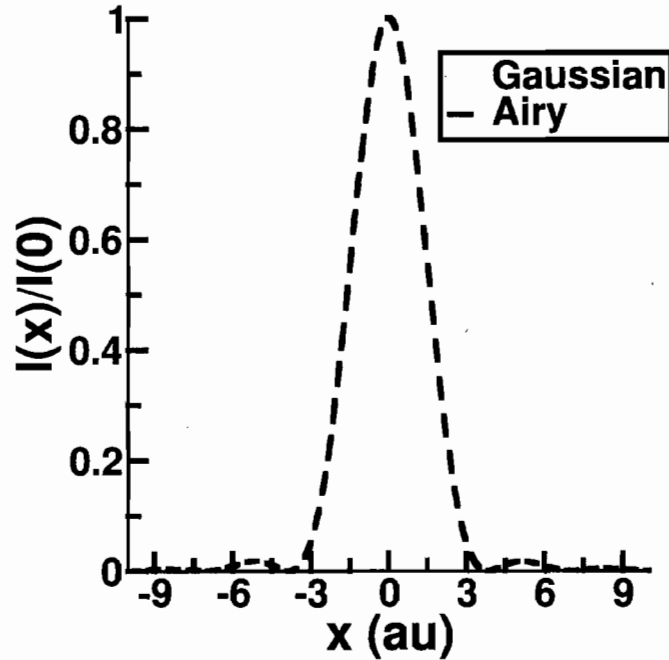


Figure 2.13: Representative plot of a one-dimensional Airy disk resulting from Fraunhofer diffraction of a circular aperture (i.e. a finite sized point source of light). Notice that the central peak of the Airy disk is well fit by a standard Gaussian ($I(x) = I_0 e^{-\frac{x^2}{2\sigma^2}}$).

Taking a time series of images of these particles and subsequently tracking them will produce a Gaussian distribution of particle positions, see Figure 2.14. The width of this distribution is the characteristic variance in the position measurements. For our microscope the variance is only $\pm 10\text{nm}$ which is an order of magnitude less than the diffraction limited resolution.

All image processing was done in MATLAB using in-house developed tracking routines written by myself and Raghuveer Parthasarathy based on previous work by John Crocker, David Grier, Eric Weeks, and Andy Dumond [35]. After images were taken on the microscope they were imported into MATLAB and a bandpass filter

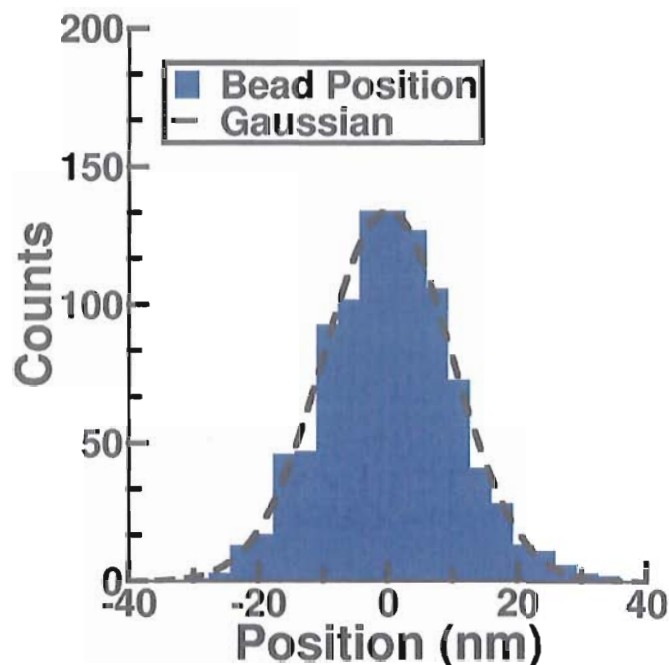


Figure 2.14: Distribution of stuck particle positions that assess particle tracking accuracy. The particle in this example is stuck to a glass surface and the variation in particle position is due to tracking error and not particle motion. The width of this distribution determines the accuracy of the tracking method, 10nm in this case.

was applied (Figure 2.15). All pixel intensity values below a user chosen value were set to zero which eliminated background noise and set a sharp boundary to particle images and an average particle size was chosen to eliminate bright objects whose size was significantly different from the particles. Next, local maxima are determined resulting in a list of x,y coordinates of individual particle neighborhoods. The center of the particles were then found by fitting a 2D Gaussian to the intensity profile in the crudely determined particle neighborhoods. Additional particle characterizations can be performed beyond the determination of particle trajectories. For example, trajectories can be filtered by velocity, power law fits, radius of gyration, or total



Figure 2.15: Data analysis flow of our video particle tracking procedure. (*Left*) raw fluorescence image of 200nm spheres bound to a freestanding lipid bilayer. The bright spots are the particles. (*Middle*) image with an intensity bandpass filter applied. All pixels with an intensity less than a user chosen threshold are set to zero. At this point the local intensity maxima are cataloged by a simple nearest neighbor comparison. (*Right*) filtered image with Brownian motion tracks overlaid. The track positions are determined by fitting a 2D Gaussian to the local intensity profile in the neighborhood of the local maxima found in the previous step. These trajectories provided position as a function of time for all particles in each sample.

duration. These additional controls eliminate errant trajectories that while imaged sufficiently, result in behavior not indicative of Brownian motion.

CHAPTER III

LIPID DERIVED DESICCATION RESISTANCE

Introduction

Tuberculosis continues to persist as a health concern in the developing world and has experienced a major resurgence in developed nations. One-third of the human population is infected with *Mycobacterium tuberculosis* (MTb), the bacteria that causes tuberculosis. Nearly two million people die each year as a result of infection [36–38]. Moreover, mycobacteria on the whole are well known to survive harsh environments including extreme bouts of dryness. Specifically, *M. tuberculosis* and *M. leprae* (responsible for leprosy) are able to withstand prolonged periods of desiccation lasting up to several months [39–45]. One may suspect the biophysical properties of MTb play a role in the persistence of this bacteria. Evidence for such a connection can be seen in the structure of the outer envelope of all mycobacteria in which includes a dense network of large fatty acids whose arrangements provides significant protection against normal permeable antibiotics and, in some cases, mechanisms for manipulating host immune response [46–48]. While a connection between the molecular composition of the mycobacterial outer membrane and bacterial robustness

has long been suspected, little is known about which specific components are important and even less is known about the protective mechanisms.

Glycolipid Derived Desiccation Resistance

Trehalose 6,6'-dimycolate (TDM, also known as cord factor) is a glycolipid present in all mycobacteria as a component of the outer envelope and is the most abundant extractable lipid at the surface of virulent MTb [49, 50]. Recently, the only mycobacterium thought to not possess TDM, *M. leprae*, was shown to in fact contain the lipid in considerable quantity [51]. Over a half-century ago, TDM was isolated and classified as a toxic glycolipid and scientific work has continued to probe TDM's impact on organisms [47, 52, 53]. Much is known of TDM's influence on animal immune response including its ability to induce granuloma formation similar to those found in organism suffering from tuberculosis [50, 54]. TDM can inhibit the trafficking of phagocytosed bacteria in macrophages [55], trigger chemokine and cytokine production [56], and dictate the morphology of mycobacteria colonies [53, 57, 58]. Perhaps the most interesting influence is TDM's ability to inhibit vesicle fusion in liposomes. This inhibition may directly explain TDM's role in preventing harmful bacteria from being destroyed during phagosome-lysosome fusion in normal macrophage function. While it is clear that TDM is of general interest for its impact on immune response, surprisingly little is known of its role outside of a host environment.

The glycan headgroup of TDM is trehalose sugar (α -D-glucopyranosyl-(1,1)- α -D-glucopyranoside). This sugar is abundant in mycobacteria as a free cytosolic agent and conjugated to various molecules in the cell envelope [59, 60]. Interestingly, free trehalose sugar is known to protect protein, membranes, and whole organisms from osmotic stresses, low temperatures, and dehydration in a host of organisms such as microbes, fungi, and plants [61]. Solutions of trehalose can stabilize dried lipid bilayer membranes and preserve them upon rehydration [62, 63]. Despite the widespread influence of free trehalose sugar, trehalose-containing glycolipids are totally absent in nature outside the mycobacteria and a few related groups [64]. The free trehalose properties described above and the significant presence of TDM in mycobacteria, led us to hypothesize that the presence of TDM may influence membrane preservation during dehydration and rehydration. The following sections detail my efforts to bring clarity to this issue and assess to what extent TDM modulates membrane response during desiccation.

Desiccation Resistance in Model Mycobacterial Membranes

Below, we detail the construction of two-dimensionally fluid, TDM-rich model membranes that mimic the structure of the mycobacterial envelope and the use of this system to measure membrane resistance to desiccation. We find that TDM and synthetic trehalose glycolipids both impart striking desiccation resistance to our

model membrane system. The resistance is characterized in two independent ways, membrane fluidity and protein binding.

Model Mycobacterial Membranes

In mycobacteria, a two-dimensionally fluid, TDM-rich monolayer sits atop a dense, hydrophobic mycolic acid layer [49, 50]. The mycolic acid layer is covalently bonded to a branched network of peptidoglycan and arabinogalactan that renders it immobile. The TDM-rich monolayer is also home to other mobile lipids and provides the interface to the surrounding environment [46, 48, 49, 56, 65–67], see Figure 3.1. To mimic this bacterial envelope, in a system that, unlike live mycobacteria, allows control of lipid composition, we created a supported monolayer system consisting of a dense, hydrophobic, and immobile layer of octadecyltrichlorosilane (OTS) that is covalently bound to a silicon/silicon oxide (Si/SiO₂) substrate on top of which a two-dimensionally fluid, TDM-rich monolayer was deposited shown in Figure 3.1. Monolayer deposition onto the supporting substrate was accomplished via Langmuir-Blodgett deposition as detailed in Chapter II. The compositional control of the fluid monolayer is used to good effect by the inclusion of fluorescent lipids, Texas Red-DHPE, and lipids with protein binding handles attached to the head groups (biotinylated lipids). The fluorescent lipids allow membrane integrity, topography, and fluidity to be imaged and measured. Biotinylated lipids provide another measure of membrane preservation in comparing protein binding levels to pre-desiccation levels. These functional lipids comprise only a small percentage of the overall

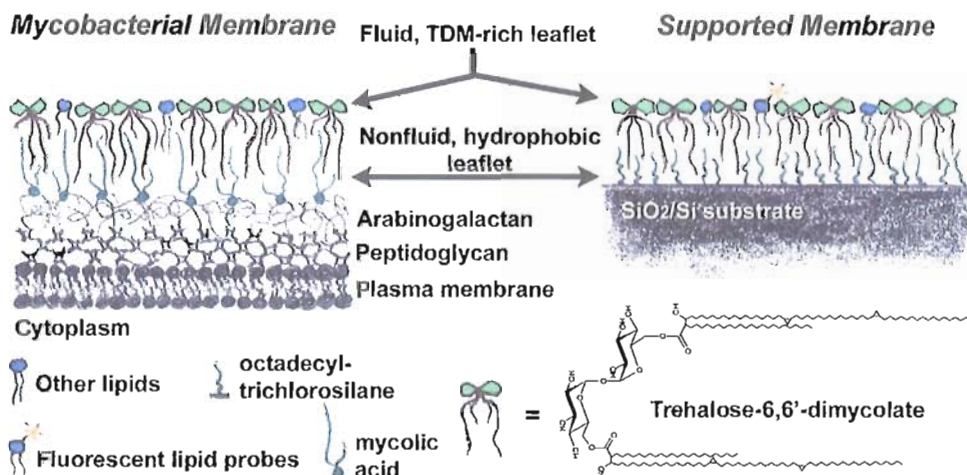


Figure 3.1: Model mycobacterial membrane schematic illustration and comparison to our experimental supported membrane system. In both, the outermost leaflet is a two-dimensionally fluid lipid monolayer rich in the glycolipid trehalose 6,6' dimycolate (TDM). Underlying this outer leaflet is a dense, hydrophobic, non-fluid monolayer composed in mycobacteria of mycolic acids covalently bound to the arabinogalactan layer underneath, and in our model platform of octadecyltrichlorosilane covalently bound to a silicon wafer. Illustration by Raghuveer Parthasarathy.

membrane, about 2 - 4%. The remainder of the membrane is made of various combinations of trehalose glycolipid and dioleoylphosphatidylcholine (DOPC), a common phospholipid. DOPC itself, as shown below, does not survive the desiccation process and allows us to assess the degree to which trehalose glycolipids provide protection during such processes.

Fluorescence imaging of the supported lipid monolayer showed uniform fields of substrate coverage. The topography was verified by Fluorescence Interference Contrast Microscopy (FLIC) performed on representative samples. The FLIC methodology is detailed in Chapter II. FLIC measurements (e.g. Figure 3.2) of 12 samples labeled with headgroup-conjugated Texas Red-DHPE probes (1 mol%) in

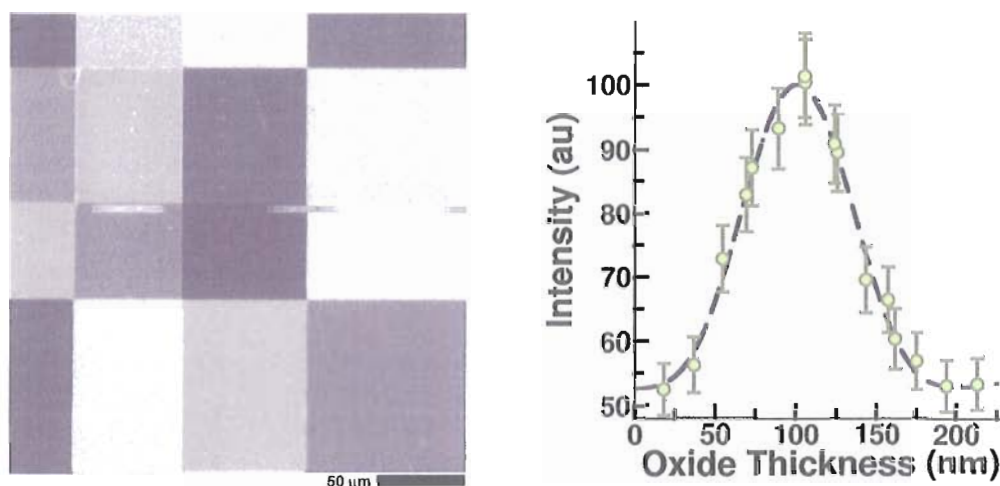


Figure 3.2: Representative data from a FLIC measurement. (*Left*) fluorescence image of a 0.99:0.01 TDM:Texas Red-DHPE monolayer. Each square represents a different oxide layer thickness that results in a different interference intensity. (*Right*) intensity data as a function of oxide layer thickness with membrane height as the only fit parameter.

TDM membranes yielded heights of 2.7 ± 1.1 nm above the oxide surface, consistent with a monolayer structure.

With the assistance of Tristan Deborde and Ethan Minot from Oregon State University, we independently verified the membrane topography using Atomic Force Microscopy (AFM), a more conventional method of determining feature heights in biological systems. The Minot group possesses significant expertise in conventional and wet AFM measurements. AFM, using a scanning cantilever, cannot provide an absolute height measure and rather it reports a difference in height between two adjacent structures. Fortunately, we were able to induce defects (holes) in TDM monolayers created as described above by cooling the samples from a deposition temperature of 35 °C to around 22 °C. The cooling process decreases the average

area per lipid in the monolayer creating gaps. At room temperature, plateaus of membrane were observed via AFM and dragging the cantilever from the top of a membrane plateau to the substrate exposed membrane hole adjacent to it provide an absolute measure of membrane height. Representative data can be seen in Figure 3.3. Membrane height, measured over multiple TDM samples, was measured to be 2.7nm with a surface roughness of 0.15nm. The roughness was assessed by calculation the standard deviation of the height in a typical $0.5\mu\text{m}^2$ patch.

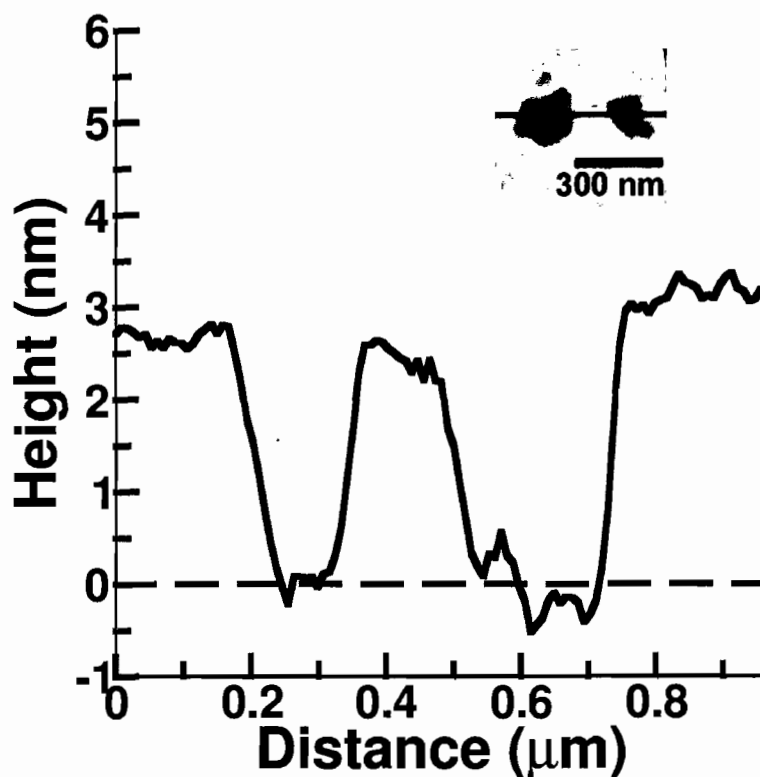


Figure 3.3: AFM measurement of a 99 mol% TDM supported lipid monolayer with room temperature induced defects (holes). The height scan is taken along the line shown in the inset. The heights measured are consistent with the presence of a single lipid monolayer.

Measurement of Desiccation Resistance

At 40 °C, TDM with 1 mol% Texas Red-DHPE forms two-dimensionally fluid supported monolayers (Figure 3.4). Images show uniform fluorescence intensity fields indicating an intact membrane and quantitative FRAP measurements reveal the recovery of photobleached regions with a diffusion coefficient, D , of $1.26 \pm 0.22 \mu\text{m}^2/\text{s}$ ($N = 16$) (Figure 3.4 a). TDM membranes are non-fluid at room temperature (22 °C) and display features indicative of a gel or solid phase, consistent with calorimetric measurements of mycobacterial envelopes that find a fluidity transition temperature above room temperature (around 30 - 35 °C) [65, 66]. The supported monolayers are dehydrated by removing them from PBS chambers, drying with a stream of nitrogen gas for 1 min, exposure to ambient air for 10 min, and then rehydrated by immersion in fresh PBS. After rehydration, the membranes again appear structurally uniform and are mobile with diffusion coefficients comparable to their original values ($1.01 \pm 0.20 \mu\text{m}^2/\text{s}$) (Figure 3.4 b). Phospholipid membranes, in contrast, are known to suffer irreparable damage upon dehydration. DOPC lipids form robust monolayers before desiccation and exhibit a normal diffusion coefficient (Figure 3.4 c), but upon desiccation and rehydration they are completely destroyed (Figure 3.4 d). FRAP measurements are not possible after rehydration given the absence of membrane on the substrate. TDM monolayers are capable of remarkable desiccation resistance not demonstrated by phospholipids. Going further, we assessed the ability of monolayers to withstand desiccation as a function of TDM content. While Figure 3.4 shows that

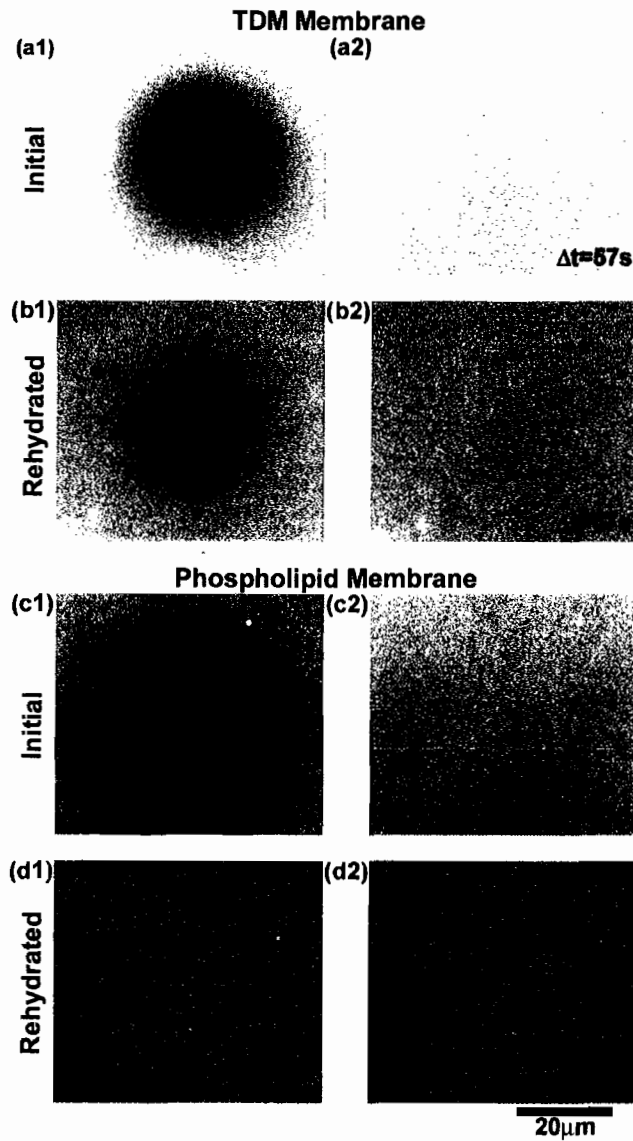


Figure 3.4: Fluorescence images of TDM and DOPC supported monolayers undergoing FRAP measurements. (a) TDM membrane FRAP before desiccation showing full fluorescence recovery and a well defined diffusion coefficient. (b) TDM membrane after desiccation and rehydration showing full fluorescence recovery and a well defined diffusion coefficient. (c) DOPC membrane before desiccation successfully undergoing a FRAP measurement with a typical $1\mu\text{m}^2/s$ diffusion coefficient. (d) DOPC membrane after rehydration showing no fluorescence even after the intensity of the image has been increased by a factor of 10 relative to that in (c).

TDM membrane can survive desiccation it is not obvious that this protection extends to other lipids that appear in non-trivial amounts in our monolayers. We constructed mixed monolayers consisting again of 1% Texas Red lipids but modified the majority components to sweep a ratio of TDM and DOPC from 1:0 to 0:1 indicating a TDM majority to DOPC majority composition, respectively. Because fluidity is a sensitive measure of membrane integrity we quantify the ratio of the diffusion coefficient after rehydration to that of before dehydration as characterized by FRAP, denoted D_R . The results of the composition dependence can be seen in Figure 3.5. As expected, pure phospholipid membranes show no recovery while pure TDM membranes show recovery as depicted previously. Surprisingly however, membrane recovery persists down to about 30 mol% TDM below which TDM no longer imparts recovery.

This sharp recovery as a function of TDM fraction has features similar to those found in percolation models that measure the spatial connectivity of elements within a network. The fit lines in Figure 3.5 come from a simulation of spatial percolation that measures the ability of a triangular lattice to have a spanning path of constituent elements as a function of the fraction of such elements present in the system. Our percolation model consists of a triangular lattice on which each site is occupied (by a TDM lipid) with probability p and then calculates the probability Q that a connected and spanning network of occupied sites exists. Extreme cases are trivial: $Q(p = 0) = 0$ and $Q(p = 1) = 1$. For $0 < p < 1$ however the form of Q is less obvious: $Q = 0$ for $0 \leq p \leq p_c$ and $Q > 0$ for $p > p_c$ where p_c is a finite critical probability. In

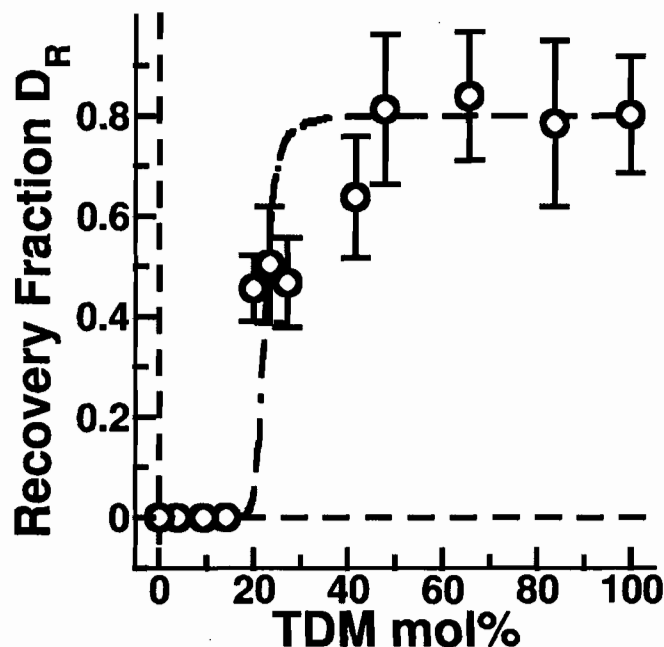


Figure 3.5: TDM desiccation resistance. The ratio D_R of the membrane diffusion coefficient after dehydration and rehydration relative to its initial value (*circles*) displays recovery over a large range of TDM concentrations. The fit curves represent calculations from 2D spatial percolation models with no adjustable parameters other than a saturation value of 0.8 (*solid line*), and with the ratio of the molecular areas of TDM and DOPC as a fit parameter (*dashed line*).

mapping this general spatial percolation to our system we directly assign the spanning probability Q onto our recovery fraction D_R since long range mobility is most likely a sign of spatial connectivity. The site occupation probability p is then mapped onto the fraction of TDM present in the membrane since desiccation resistance is derived from these lipids alone. Analytical forms of $Q(p)$ do not exist in general but we simulated site-percolation on a 2D triangular lattice, the details of which can be found in Appendix .1. As can be seen in Figure 3.5, the data are well fit by a percolation model.

We can improve our percolation fit by making a more exact mapping from p to fraction of TDM. In the basic percolation model, every lattice site is the same size and this is not consistent with the experimental model system. TDM lipids, due to the large trehalose headgroup, have a larger area in the monolayer when compared to DOPC. We can account for this area difference in our mapping as follows: $m = p/[p + (1 - p)r]$ where r is the ratio of the area per TDM molecule to that of DOPC. This mapping is equivalent to saying that each TDM molecule occupies r lattice sites rather than 1, which would be the equal area case. Experimentally we know $r > 1$ [68] and since p_c for a $r = 1$ system would be 0.5, we expect the transition to occur at $m < 0.5$. Using this mapping, the fit line in Figure 3.5 shifts to the left, indicating the need for fewer TDM lipids to span the same distance given their bigger size, aligning quite well with the data. Literature values of the area per lipid of TDM in a monolayer are $A_{\text{TDM}} = 1.87, 1.35, 1.60\text{nm}^2$ [69–71] providing an average of $A_{\text{TDM}} = 1.61\text{nm}^2$ and $r = 2.26$. While this correction yields a better fit (Figure 3.5 gray line) we can improve it further by allowing the ratio r to be a fit parameter. Doing so yields $r = 3.24$ and $A_{\text{TDM}} = 2.30\text{nm}^2$ which is reasonable given the spread in the literature values and reports of TDM-phospholipid compaction in mixed monolayers at air/water interfaces [69].

While TDM recovery data are well fit by a percolation model it is by no means certain that spatial connectivity of TDM within the monolayer is underlying mechanism of desiccation protection. In fact, the area per lipid may be a proxy

for a given number of interactions TDM can form with neighboring lipids. In the following sections we detail the synthesis and characterization of synthetic trehalose glycolipids whose size and structure differ significantly from that of TDM. Comparing the extent to which these synthetic lipids confer desiccation resistance to other lipids allowed us to test the robustness of such behavior and the validity of the percolation interpretation.

Synthetic Trehalose Glycolipid Derived Desiccation Resistance

Beyond its importance for microbiology, the desiccation resistance observed with TDM points out a previously unrealized physical capability of lipids. Our experiments with TDM mark the first discovery of dehydration resistant lipids. Understanding its nature, for example the relative importance of the conjugated disaccharide versus the acyl chains, will broadly impact physical chemistry and soft condensed matter physics. Synthetic trehalose glycolipids can provide a powerful tool for addressing mechanistic questions. Control of molecular architecture can delineate the structural features responsible for the behaviors exhibited by TDM, illuminating the biophysical chemistry employed by an important pathogen. The control afforded by synthetic lipids can also open doors to the engineering of desiccation resistance into lipid membranes used for a wide variety of biotechnological applications, for example supported-membrane-based sensors [11, 72] and liposome-based drug delivery [73, 74].

In conjunction with our collaborators, we have created a set of synthetic trehalose glycolipids that incorporate a single trehalose disaccharide conjugated to different lipid chain structures (Figure 3.6). Trehalose glycolipid synthesis was carried out by Zsofia Botyanszki and David Rabuka of Carolyn Bertozzi's group at the University of California, Berkeley. Members of the Bertozzi group are experts in sugar chemistry, a field known to be quite difficult. Detailed synthesis procedures can be found in [75]. The only persistent structural feature among these glycolipids is the trehalose headgroup. We incorporated these trehalose glycolipids into two-dimensionally fluid supported lipid monolayers that structurally resemble the outer envelope of mycobacteria, as in previous studies of TDM.

Measurement of Desiccation Resistance

Measurements of desiccation resistance were performed as per the TDM and phospholipid membranes described earlier consisting of 0.99-X:X:0.01, DOPC:trehalose glycolipid:Texas Red-DHPE using the supported monolayer architecture described in Chapter II and detailed in the preceding sections of this chapter. All samples from $X = 0$ to 0.99 trehalose glycolipid showed bright, uniform fields of fluorescence and yielded diffusion coefficients on the order of $1\mu\text{m}^2/\text{s}$ as measured by fluorescence recovery after photobleaching (FRAP), indicating intact and well formed monolayers (Figure 3.7 a and c).

At $X = 0.99$, the trehalose glycolipids **1** and **2** (Figure 3.6) showed uniform, bright fields of fluorescence and 2D mobility after rehydration. In contrast, DOPC

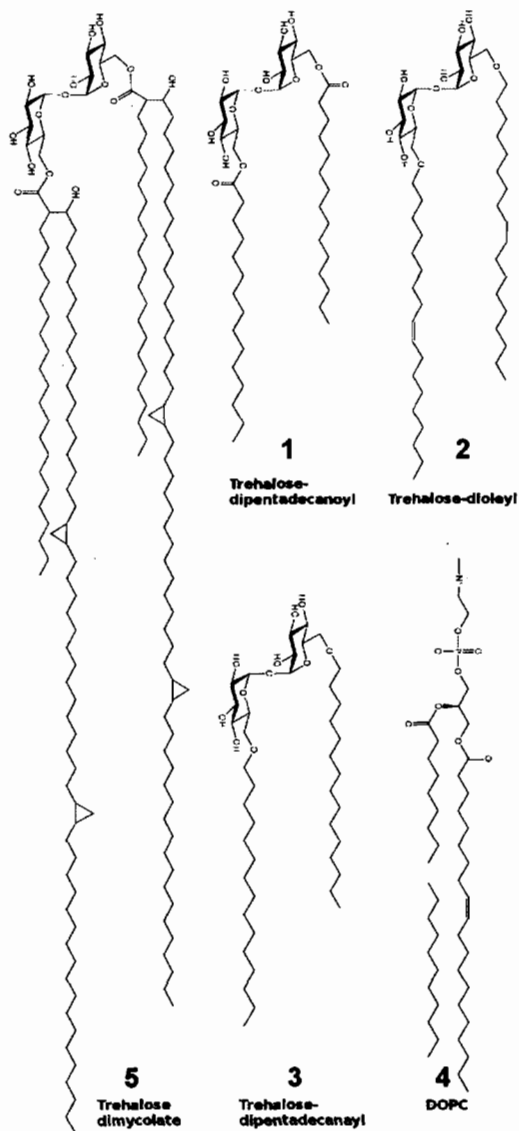


Figure 3.6: Synthetic trehalose glycolipid structures. (1,2,3) Synthetic trehalose glycolipids intended to provide desiccation protection. (1) Ester linked trehalose-dipentadecanoyl. (2) Trehalose-dioleoyl. (3) Ether linked trehalose-dipentadecanoyl. (4) DOPC, a common phospholipid with similar hydrophobic tail structure to synthetic compounds 1, 2, and 3. (5) Trehalose dimycolate, desiccation resistant lipid found in all mycobacteria.

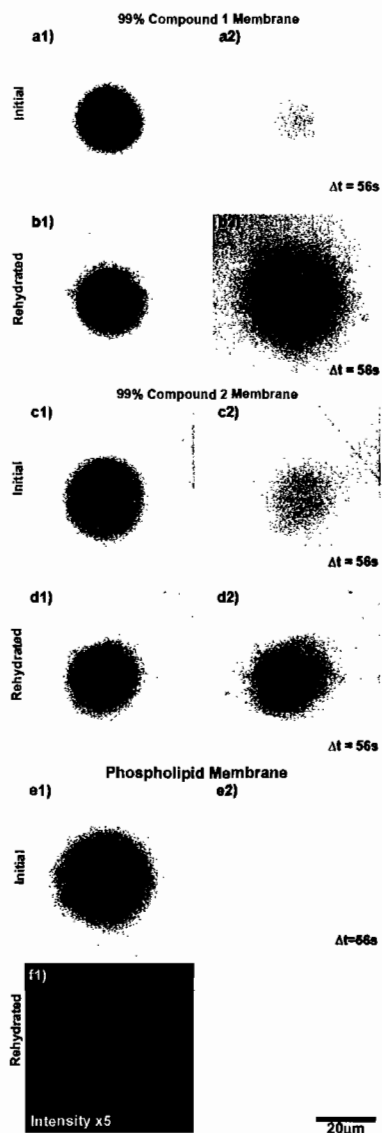


Figure 3.7: Membrane fluidity and dehydration resistance quantified by fluorescence recovery after photobleaching (FRAP) in synthetic trehalose glycolipid monolayers. (a-e) Fluorescence images of supported monolayers containing 1 mol% Texas Red-DHPE. Initially, images of 99 mol% synthetic trehalose glycolipids (a and c) and 99 mol% DOPC (e) display intact monolayers with characteristically bright and uniform fields of fluorescence. (a2,c2,e2) When the monolayers are photobleached in a defined circular region, they recover a uniform field of intensity, indicating fluidity. (b and d) After dehydration and rehydration, FRAP images of 99 mol% trehalose glycolipid display a similarly intact, bright, and fluid monolayers. (e) Monolayers of 99 mol% DOPC show no measurable intensity above background noise after dehydration and rehydration and are destroyed by the desiccation process. The intensity of f has been increase by a factor of 5 relative to e.

($X = 0$) membranes were destroyed by the desiccation process, as expected. The ratio of the diffusion coefficient after rehydration relative to the initial value before dehydration gives a quantitative measure of recovery, which we refer to as the recovery fraction (D_R). For all $X = 0.99$ trehalose glycolipid samples examined, D_R was greater than 0.50 indicating the synthetic trehalose glycolipids successfully reproduce the desiccation resistance that previously had only been observed with TDM.

A concentration series with synthetic trehalose glycolipids **1** and **2** over the range $X = 0$ to 0.99 reveals strikingly similar recovery curves to those measured with TDM (Figure 3.8). The synthetic lipids provide no protection below a well defined critical fraction, p_c , and, above p_c , D_R rises indicating protection of the membrane against dehydration. The saturated step behavior has a form similar to many percolation phenomenon and a fit to a percolation model gives values of p_c that are very similar for the three lipids, 0.23 for **1**, 0.17 for **2**, and 0.20 for TDM, each with an estimated uncertainty of $\pm 3\%$. The robustness of the protecting ability was examined by subjecting synthetic trehalose glycolipid monolayers with $X = 0.90$ to an extended dehydration time of two weeks. The samples were dehydrated using the normal process and left exposed to ambient air for a further two weeks. Upon rehydration, the samples recovered with D_R greater than 0.6.

We examined synthetic trehalose glycolipids with two 8 carbon and single 15 carbon hydrophobic chains, otherwise identical in structure to compound **1**. Over the full range $X = 0$ to 0.99 we found no protection against desiccation (data not

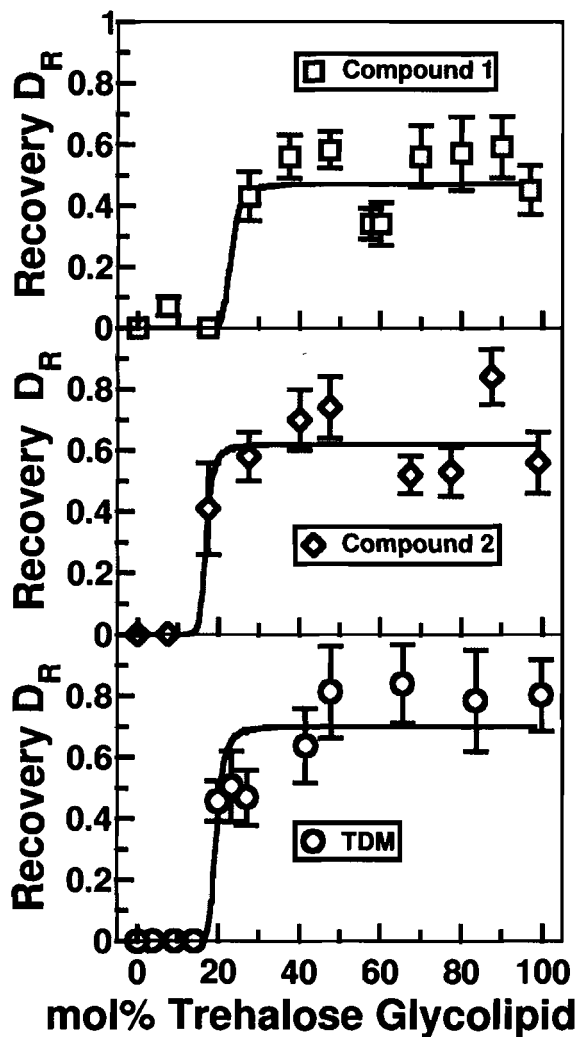


Figure 3.8: Comparison between TDM and synthetic trehalose glycolipids. The ratio, D_R , of the membrane diffusion coefficient after rehydration to its initial value (symbols) shows recovery of the membrane above a critical fraction. The curves represent simulated percolation on a triangular lattice with the saturation, p_{sat} , and critical fraction, p_c , as fit parameters. In the fit, the mapping from site occupation probability to mole fraction includes the ratio of the area per trehalose glycolipid to the area per DOPC. Synthetic trehalose glycolipids (*top* and *middle*) show the same recovery behavior as the previously investigated TDM (*bottom*) despite their structural differences.

shown). However, pressure versus area isotherms of monolayers containing the 8 carbon lipids at the air/PBS interface prior to deposition showed a strong decrease in surface pressure over time indicating that glycolipids were leaving the interface. The critical micelle concentration (CMC), for 8 carbon lipids is 0.3mM while for the single chain 15 carbons lipids the CMC is $\approx 0.1\text{mM}$ [76], well above the lipid concentrations present in this studies. The short chain and single chain lipids are incapable of stable incorporation into the membrane, thereby, explaining the lack of desiccation protection.

In addition to assessing recovery via lipid mobility, we also measured the overall fluorescence intensity. Compared to mobility, this is not a reliable marker of membrane integrity due to the sensitivity of fluorescence intensity to the environment. We find varying degrees of photodamage while in the dry state. Still, the overall brightness for the membranes that do not recover after dehydration and rehydration is small, less than 5% of the original brightness whereas membranes that survive dehydration and rehydration recover over 60% of their original brightness. This result corroborates the recovery behavior indicated by the mobility, and also confirms that the fluorescent probes are not incorporating into the solid-anchored OTS monolayer.

Evidence Against a Percolation Model

The synthetic trehalose glycolipids confer dehydration resistance to membranes, with very similar behaviors as natural TDM. The synthetic lipids and TDM have identical trehalose headgroups but different hydrophobic chains in terms of chain

number, length, and linkage. Therefore, the dehydration resistance conferred by TDM appears to be determined by trehalose, with no apparent role for the chains in this process other than enabling stable membrane anchoring. The protective behavior must be derived from interactions mediated by the trehalose headgroup and surrounding molecules. Exploring the molecular underpinnings of these interactions promises to be a fascinating avenue for the future studies. Free trehalose has been studied extensively, and its mechanism of protection likely involves the disaccharide affecting the formation of a glassy state and/or replacing hydrating water molecules via the formation of hydrogen bonds with the protected species. However, the relative importance of these effects remains undetermined.

A major difference between the activities of free trehalose and the trehalose glycolipid is that in the latter the disaccharide is of course not free but bound. This will undoubtedly constrain the interactions between the sugar, whose rotational and translational freedom is limited, and the nearby phospholipids. Many questions related to this remain open: Is there a "mapping" that can be constructed between 2D concentrations of trehalose glycolipids and 3D concentrations of free trehalose that lead to similar behaviors? How many phospholipids can one lipid-conjugated trehalose interact with? Notably, both linkages probed in this study connect to trehalose to the hydrophobic chains at two sites; a singly connected linkage, though synthetically challenging, may confer more degrees of freedom to the disaccharide.

The membrane recovery versus trehalose glycolipid fraction appears well fit by the percolation form described in the TDM section previously, but this apparent agreement illuminates an important flaw in the percolation model. The essence of the percolation model is as follows: we hypothesized that desiccation resistance occurs if, at any instant in time, the trehalose glycolipid forms a connected network spanning the membrane. As with all percolation phenomena, there is a critical area fraction associated with the existence of this spanning network, which translates to a critical composition in a manner determined by the relative molecular areas of the trehalose glycolipid and the phospholipid (DOPC). Simply by virtue of geometry, larger glycolipids are able to form networks spanning the membrane at lower molar fractions than smaller glycolipids. The synthetic lipids have much smaller hydrophobic chains, and presumably smaller areas, than TDM (Figure 3.6). This would lead us to expect larger p_c values for the synthetic trehalose lipids than for TDM. Specifically, the similarity in size between compounds **1**, **2**, and DOPC would suggest $p_c \approx 0.5$. However, we find that the critical synthetic trehalose glycolipid fractions, p_c , are the same as that of TDM to within our estimated composition uncertainty of $\pm 3\%$ (Figure 3.8). Not only does the invariance of p_c with lipid structure argue against a percolation transition, it also strongly implies that structural transitions in lipid packing do not determine p_c , as these would also show strong dependence on the glycolipids' molecular structure.

The similarity of p_c across trehalose glycolipids suggest a different mechanism. The headgroup, a single trehalose disaccharide, is the same for all the compounds examined. The sugar may be forming connections with a specific number of neighboring lipids within the membrane, most probably through hydrogen bonding. Dehydration resistance of the membrane may emerge when this local bonding interaction is sufficient to involve the overall lipid population. In this picture, the onset of protection should be independent of the molecular size or chain structure, consistent with the observations. The steepness of the rise of D_R above its threshold remains surprising, and may indicate some degree of cooperativity in the glycolipid-phospholipid interactions.

Summary and Outlook

The trehalose glycolipids described here are the first reported lipids that confer desiccation resistance to membranes. This behavior not only illuminates biophysical properties relevant to mycobacteria, but also opens doors to exploiting these unique properties in various contemporary areas of lipid research. The formation of liposomes and DNA-lipid complexes, for example, both very important to drug and gene delivery applications, depends sensitively on lipid structure. The advent of synthetic, dehydration resistant trehalose glycolipids may allow the creation of desiccation resistant liposomes, bilayers, and other structures. The independence of our data on hydrophobic chain architecture reveals that molecular structure can be tuned for

specific applications independent of the trehalose-derived protection. Furthermore, it suggests routes to enhanced protection by engineering multiple disaccharides per molecule or by developing a better molecular-level understanding of trehalose-phospholipid interactions.

The next steps in the characterization work presented here involve further elucidation of the mechanism of desiccation resistance. Since we have provided ample evidence that the lipid tail groups do not influence the resistance behavior we must look to the lipid head group. The sugar head group has a number of hydroxyl groups that may provide stabilizing hydrogen bonds to neighboring lipids. To discern if the hydroxyl groups alone are capable of providing the observed resistance we are faced with the synthetic chemistry problem of changing the number of available hydroxyl groups. Initially, one could substitute the hydrogens in these groups with deuterium thereby hydrogen bond vibrational frequency of the now OD groups on the sugar. The OD bonds may be identifiable in infrared reflection absorption spectroscopy or related techniques allowing for the detection of such stabilizing bonds in the dehydrated state.

A different approach is to engineer trehalose glycolipids that have two sugars per head group effectively doubling the number of hydrogen bonds the lipid can make with surrounding lipids. If hydroxyl groups are the primary desiccation protection providers a corresponding decrease of critical trehalose glycolipid fraction should be observed. The experimental platform presented here also lends itself to further explorations of the mycobacterial outer envelope. The inclusion of other

mycobacterial lipids will allow for precise characterizations of their properties and possibly provide explanations pertaining to their role in desiccation resistance and other phenomena. Even in the absence of a mechanistic explanation, lipid derived desiccation resistance, as characterized in this work, stands firm as an important technological tool in the creation of new, liposome based drug delivery and protection.

CHAPTER IV

VISCOELASTICITY IN LIPID BILAYERS

Introduction

Membrane mobility is an important property for cell structure and function. While the ability molecules to diffusive in lipid membranes is well known [77–84], little is understood about the underlying material properties that govern the dynamic movement and interactions in membranes. General consensus holds that membranes are two-dimensional viscous fluids but little has been done to critically examine this assertion. For example, a viscoelastic membrane would also be capable of displaying the observed diffusive motion in membranes. To date, measurements by various groups [85–89] of lipid membrane viscosity show no convergence to agreeable values nor do they differentiate between viscous and viscoelastic models. Compounding the problem, current measurement techniques remain imprecise and low throughput.

Determining whether lipid membranes are viscous or viscoelastic is an important step in understanding not only the character of membrane fluidity but more simply how to even measure this fundamental property. The classification and characterization of membranes as viscous or viscoelastic fluids opens the door for further investigations of many membrane properties such as phase behavior, diffusive

motion, and lipid-protein interactions. Efforts to model lipid and protein interactions in membranes have already begun to probe the importance of mobility and posed questions whose answers hinge on a reliable method of measuring mobility [90–92].

We adapt recently developed microrheological techniques to measure freestanding lipid bilayer complex shear moduli, properties that describe fluidity. This technique provides information about membrane viscoelasticity over a broad frequency range that, in principle, can be tuned to observe material properties relevant to protein conformational change times. Many membrane associated proteins have conformational change times from 10^{-1} to 10^{-9} s [93–98]. Such a wide range of times requires a mapping of membrane material response across an equally wide range of perturbation frequencies to accurately characterize the physical environment experienced by proteins.

Free-standing Lipid Bilayers

Working with a cell free lipid bilayer that allows for compositional control is a requirement to understanding lipid membrane fluidity. The complexity and lack of certainty regarding the contents of a live cell membrane make it difficult to attribute any measured behavior to a particular membrane component. A freestanding lipid bilayer, shown schematically in Figure 2.2 and detailed in Chapter II, is a useful system that allows for many different combinations of constituent lipids. This compositional control allows us delineate the contributions of different lipids to

membrane fluidity. Moreover, the lack of support contact in freestanding lipid bilayers further isolates lipid contributions to membrane fluidity since it is known that contact with supporting substrates influences the lipid diffusion coefficient, membrane-protein interaction, and membrane geometry [9–11].

Freestanding lipid bilayers are prone to instability if subjected to forces perpendicular to the membrane plane. Given this unfortunate fragility, care must be taken in both preparation and measurement to minimize these destructive forces. This includes reducing convective flows in preparation and measurement buffers by matching their temperature and keeping it constant. When washing or transferring the membrane, care must be taken to move the substrate with the least amount of drag possible (e.g. holding the substrate parallel to the direction of motion). Much of the fragility seems to be mitigated by taking great care to densely pack the substrate with hydrophobic molecules. Further progress can be made by using a high concentration of hydrophobic oil during the preparation process and waiting overnight for the oil to diffuse out of the space between bilayer leaflets.

Membrane Material Properties

Lipid Membrane Phases

Membranes, as 2D fluids, are capable of undergoing a number of phase transitions modulated by composition and environmental variables. One particular phase transition is the liquid-ordered to liquid-disordered transition [99]. Simple

freestanding lipid bilayers composed primarily of one or two lipid species can exist in two distinct phases characterized by the alignment of their lipid tails. In the liquid-ordered phase (low temperature), lipid tails in opposite monolayers of a freestanding lipid bilayer align with each other [100] and the phase is known to be crystalline [101]. The ordered phase is characterized by a gel-like response in which the lipid diffusion coefficient is lower than in the higher-temperature disordered phase. The disordered phase is defined by the lack of alignment in lipid tail groups measured by the absence of a well defined structure factor [102, 103].

Classification of this melting transition as first- or second-order is still uncertain [99, 104–108]. While being a first- or second-order phase transition does not change any of the data presented, it may influence the interpretation of the data. Recall that first-order phase transitions typically show no sign of a phase transition arbitrarily close the transition temperature and allow two-phase coexistence near the transition. Second-order transitions are observably continuous (in the first derivative of free energy) and do not allow for two phase coexistence.

Viscoelasticity

Viscoelasticity represents the idea that a material can simultaneously display viscous flow and elastic response, and one or the other of these may be dominant at different timescales. Some of the more popular examples of viscoelasticity are the non-Newtonian fluids like cornstarch-in-water mixtures. These fluids flow like water when slowly poured but feel hard when hit quickly. The key difference

between these behaviors is the timescale (or frequency) of the material perturbations. Slow perturbations, pouring or stirring, encounter a viscous response while fast perturbations like hitting or dropping encounter an elastic response. In the following section we will explore how conventional measurements of viscous and elastic fluid properties are measured and how they need to be modified for lipid membrane investigations.

Microrheology

Particle Tracking Microrheology

Rheology is the study of material flow. Conventional rheology measurements are conducted with a rheometer [109]. This device confines a small amount of liquid between two plates and uses those plates to shear the liquid at a defined frequency. The rheometer then measures the force or pressure response, both viscous and elastic, of the fluid. This technique, while useful, is not applicable to freestanding lipid bilayers. The freestanding lipid bilayers are about 5nm thick and 125 μ m across and bringing two metal plates in shearing contact with the surface is impossible. Moreover, perturbations affected by a rheometer are, in general, much larger than $k_B T$ and would destroy the membrane.

Microrheology, a recently developed field, was created, in part, to address the issues facing rheological measurements in small samples of complex fluids [110]. In microrheology, small tracer particles are attached to the sample of interest and

their Brownian motion is imaged at high speeds, in our case biotinylated lipids in a freestanding lipid bilayer. As detailed in Chapter II, we can extract particle, and hence lipid, Brownian motion trajectories using video particle tracking. These tracks yield mean squared displacements (MSD) that are representative of the entire collection of thermal perturbations and other interactions experienced by the particles and their lipid anchors.

While the MSD itself is an interesting function, we are more interested in the rheological properties of freestanding lipid bilayers that one normally attains through the use of a rheometer. In particular, we want to measure the complex shear modulus, denoted as $G^*(\omega)$. This function describes the freestanding lipid bilayer's viscoelastic response to perturbations as a function of frequency in the form of an applied stress divided by the resulting material strain [111]. To calculate $G^*(\omega)$ from measured MSDs we follow the procedure laid out by Mason [112]. The relationship between the two functions is set by the generalized Stokes-Einstein equation (GSE):

$$G^*(\omega) = \frac{k_B T}{\pi a \omega \mathfrak{F}\{\langle \Delta r^2(t) \rangle\}} \quad (4.1)$$

where $\Delta r^2(t)$ is the MSD, a is the diameter of the probe particle, and \mathfrak{F} denotes the Fourier transform. It is worth remembering at this point that the MSD is generated by Brownian motion which can otherwise be described as thermal white noise. The motion of the bound particles and lipids is dictated by the simultaneous thermal perturbations of magnitude $k_B T$ at all frequencies.

However, unlike conventional rheology, microrheology does not actually measure a physical force but only the motion of particles and lipids subjected to forces. Equation 4.1 provides a link between MSDs and the complex shear modulus and a detailed derivation can be found in [112]. Briefly, linear viscoelasticity in an isotropic material can be represented by a single scalar function $G_r(t)$, the normalized relaxation of stress due to an applied strain, as dictated by the fluctuation dissipation theorem (FDT) [113–115]. The FDT relates spontaneous thermodynamic fluctuations in a system to their linear response and the scalar function $G_r(t)$ represents the dissipation of random thermal fluctuations in any system. The connection between the MSD and the complex shear modulus is made possible by the FDT.

Roughly, the FDT allows one to recast the dissipative response of a system as a correlation function within the system. In our case the dissipative response, $G_r(t)$, is recast as a MSD, our material correlation function. To transition from $G_r(t)$ to $G^*(\omega)$ (the Fourier transform of $G_r(t)$), we need only assume that the local viscoelasticity around the lipid probe is the same as the macroscopic viscoelasticity and we can then calculate $G^*(\omega)$ directly from the MSD arriving at Equation 4.1. A useful interpretation of the complex shear modulus is found in considering both the real (elastic modulus) and imaginary (viscous modulus) parts separately, $G^*(\omega) = G' + iG''$. These two moduli are connected by the Kramers-Kronig relations and contain all of the information found in $G_r(t)$ but separate the solid-like (G') and liquid-like (G'') responses.

Equation 4.1 is not straightforward to implement experimentally. The Fourier transform, as defined in [112], requires infinite time domain measurements to produce the corresponding infinite frequency domain. Experimentally, we are limited to only a few decades of time measurements and direct Fourier transforms of such limited data sets yields inaccurate results particularly near frequency extremes. We implement the approach taken by Mason and estimate the Fourier transform rather than performing the explicit Fast Fourier Transform (FFT). The estimation assumes only that the measured MSDs are locally well fit by a power law in time over some temporal range. Since the MSDs are the result of Brownian motion in a viscoelastic system they will be power laws in time with their power ranging from 0 (elastic) to 1 (viscous) rendering the assumption valid. We take additional care in our data collection to ensure that only MSDs that are well fit by a power law in time are kept.

Again, the details of the method can be found in [112] but the general approach is to locally expand the MSD around the frequency of interest (dictated by the actual experimental time sampling), keep the leading term of the expansion, Fourier transform the expanded term, and substitute the transformed expansion into the GSE. By keeping only the leading term in our expansion we assume that contributions to the Fourier transform of a particular data point from frequencies far away from that point do not significantly contribute to the complex shear modulus. That is to say, the MSD measured at a particular time is assumed to be generated by thermal perturbations in a small frequency range and not a collection of perturbations from

many different frequencies. The final expression is

$$|G^*(\omega)| \approx \frac{k_B T}{\pi \alpha \langle \Delta r^2(1/\omega) \rangle \Gamma[1 + \alpha(\omega)]} \quad (4.2)$$

$$\alpha(\omega) \equiv \frac{d \ln \langle r^2(1/\omega) \rangle}{d \ln(1/\omega)} \quad (4.3)$$

where Γ is the gamma function and $\alpha(\omega)$ is the Fourier transform of the frequency dependent power of the first term in our MSD expansion. The approach outlined here have been well-tested in 3D complex fluids [112, 116, 117].

Controls and Tests

Given the implementation of Fourier transform estimations, use of MSDs in place of force measurements, and the relative youth of the microrheological field, the validity of our measurements benefit from testing of our methods. We assess our precision by simulating MSDs in viscoelastic systems and our accuracy is determined by performing microrheology on viscous and viscoelastic fluids that have been well characterized. These tests allow us to assess the capabilities and limitations of our measurements to not only assure the validity of the work presented here but also to establish our method as a more general platform to measure membrane fluidity.

A simple analytical model of linear viscoelasticity is the so-called Maxwell material (Figure 4.1) consisting of a spring (elastic constant k) connected in series to a viscous dash pot (viscous drag coefficient b). The analytical representation of the complex

shear modulus components in this system is quite simple

$$\begin{aligned} G'(\omega) &= \frac{(\omega\tau_m)^2}{1 + (\omega\tau_m)^2} \\ G''(\omega) &= \frac{\omega\tau_m}{1 + (\omega\tau_m)^2} \end{aligned} \quad (4.4)$$

where $\tau_m \equiv 1/\omega_c = b/k$, is the inverse of the crossover frequency below which G'' dominates and above which G' dominates, see plot in Figure 4.1. The simplicity of this model makes simulating the diffusion of small particles in such a material straightforward. We proceed by generating particle trajectories via the following equation of motion:

$$0 = -kx + -b\dot{x} + Z(t) \quad (4.5)$$

where k is the elastic spring constant, b is the viscous drag in the dash pot, and $Z(t)$ is the random thermal perturbation inherent in Brownian motion.

We chose our drag coefficient, b , to achieve a simulated particle diffusion coefficient representative of the diffusion measured in our freestanding lipid bilayers (about $1\mu\text{m}^2/\text{s}$). We then tune our choice of k to produce a crossover frequency into our experimentally accessible range. MSDs generated by this simulation are then analyzed by the method outlined previously. As illustrated in Figure 4.1, our measurement system does indeed reproduce the characteristic Maxwell material viscoelasticity. As noted in [111], ω_c is a ratio of b and k . We can control the value of the ω_c in our simulations by changing the relative magnitudes of b and k which in turn shifts the crossover frequency.

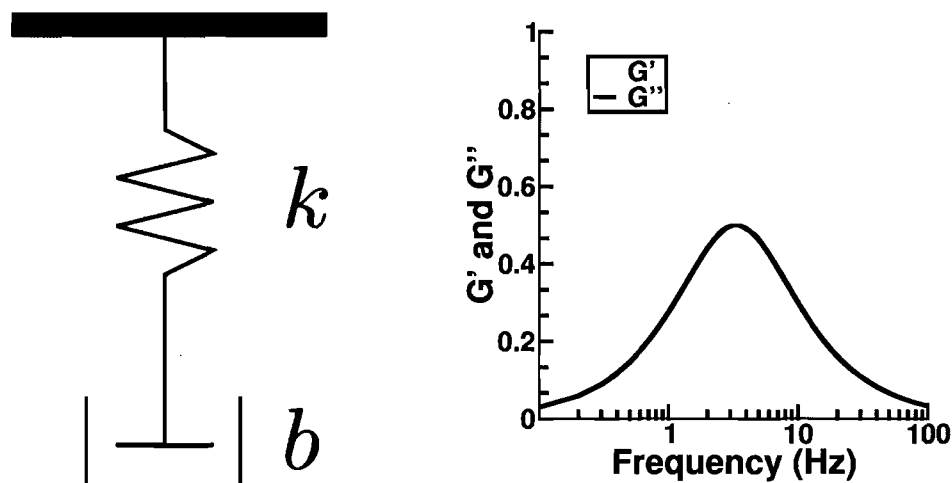


Figure 4.1: (*Left*) schematic illustration of the mechanical representation of a viscoelastic Maxwell material. This material clearly separates the elastic (spring) and viscous (dash pot) contributions of the material. (*Right*) plot of the storage (G') and loss (G'') moduli for a Maxwell model. The unique shape of the moduli provide two distinct regions of frequency response by the material. At low frequency the loss modulus dominates providing viscous behavior while at high frequency the storage modulus dominates resulting in elastic behavior with a well defined crossover point.

Going further, we can use simulations to assess the sensitivity of our measurements to actual data frame rates. Passive microrheological measurements often need large amounts of data to overcome the inherent noise in Brownian dynamics. We generated a high frame rate data set and selectively reduced its sampling rate to produce data seemingly less accurate. Subsequent analysis of these sets expose differences in their complex shear moduli manufactured by our measurement technique and not present in the data (Figure 4.2). The differences are most pronounced at the frequency extremes which is to be expected given the involvement of a Fourier transform in our analysis. Fortunately, the most accurate frequency range surrounds the crossover frequency and the overall variation is small compared to the magnitude of the individual moduli.

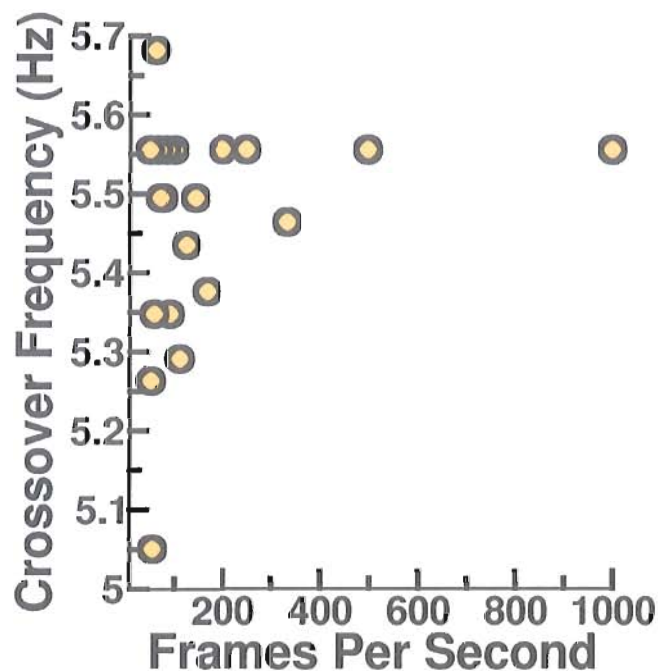


Figure 4.2: Frame rate dependence of a Maxwell material simulation. Sampling a single simulation at multiple frames per second reveals the sensitivity of our analysis to data frame rate. As the plot shows, the crossover frequency, the point at which $G' > G''$, is precisely determined at most frame rates. The crossover frequency for this simulation is $5.46 \pm 0.14\text{Hz}$ indicating a 3% error.

While this result speaks for the precision of our system it does not definitively assess its accuracy. Can we use this system to reliably produce not just the same measurement given a single set of inputs but rather make a single measurement that correctly characterizes the viscous or viscoelastic response measured by an independent method? To answer this question we turned to two fluids that have both been well characterized by bulk rheology. A mixture of 40% glycerol in water produces a purely viscous fluid. Creating mixtures of 40% and 20% glycerol in water results in a fluid with a typical embedded particle diffusion coefficient on the order

of that in our lipid bilayer samples . Particles of size 200nm were mixed in with the samples. Particle Brownian motion was recorded at 200 frames per second and the resulting MSDs were extracted. As can be seen in Figure 4.3, throughout the entire frequency range the viscous modulus dominates the elastic modulus in agreement with bulk measurements. However, at the high end of the frequency range we can see deviations from the bulk measurements. While there should be no crossover present, the two moduli seem to be approaching such a scenario. We define the reliable range as all frequencies for which the derivative of the loss modulus with respect to frequency is greater than the derivative of the storage modulus with respect to frequency and for which $G' > G''$. From Figure 4.3, we have a reliable window of 0.1 to 33Hz. The experiment was repeated using 20% glycerol in water and the results were the same.

We also performed the measurements on a viscoelastic gellan gum called Kelcogel. This substance has been characterized by both bulk rheology and microrheology [118]. Our sample, consisting of 0.1% Kelcogel in water, was prepared as described in [118]. Briefly, 20mg of Kelcogel powder was dissolved in 20ml water at 80 °C and 200nm fluorescent microspheres were added. The gellan gum was then cross linked with the addition of 100mM NaCl solution and cooled to room temperature. Particle Brownian motion was again imaged at 200 frames per second and MSDs were subsequently extracted. The results of microrheological analysis (Figure 4.4) show viscoelasticity and demonstrate that our method is proficient at extracting viscoelastic behavior from this system.

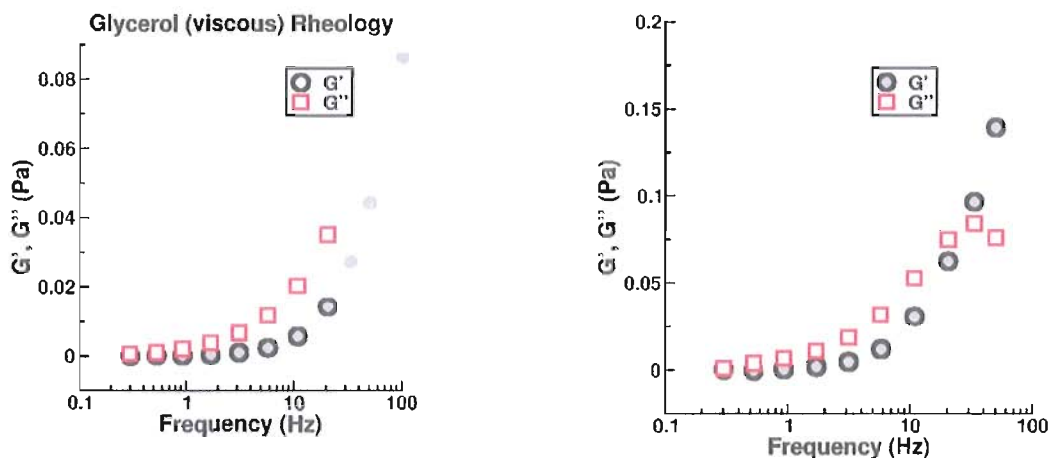


Figure 4.3: Microrheology of a common viscous fluid. (*Left*) complex shear modulus of a 40% glycerol in water solution as measured by our microrheological methods. Over two decades of frequency the loss modulus dominates the storage modulus. (*Right*) derivative of both the storage (G') and loss (G'') moduli with respect to frequency. Above 33Hz the data show the slope of G' becoming greater than the slope of G'' . Glycerol is a well characterized viscous fluid in this frequency range and as such we can use deviations from established measurements as a test for accuracy in our method. From this plot we can choose a reliable window of 0.1 to 33Hz.

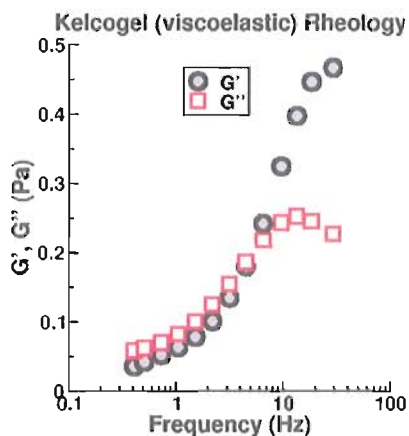


Figure 4.4: Microrheology of a viscoelastic fluid. Complex shear modulus of a 0.1% Kelcogel in water solution. Viscoelastic behavior is measured by our method and is consistent with previous measurements [118].

Viscoelasticity in Lipid Bilayers

Freestanding lipid bilayers were deposited as described in Chapter II consisting of 0.5 mol% Texas Red-DHPE, 3 mol% Biotinyl-Cap PE, and 96.5 mol% of one or a combination of the following lipids: DOPC, DMPC, DLPA, and DNPC (see Chapter II for full chemical names). Mixtures of DOPC/DMPC and DOPC/DMPS were made to bring the melting transition of DMPC and DMPS close to room temperature; DOPC concentrations were less than 9 mol%. Fluorescent, 200nm, neutravidin coated nanoparticles (purchased from Invitrogen) were incubated with these bilayers overnight. Freestanding bilayers were washed of unbound particles (with a typical bound density of 20-50 particles per $125\mu\text{m}$ patch) and transferred to fresh buffer before imaging (see Chapter II for experimental details).

For each bilayer, the temperature was increased above the lipid melting temperature using a temperature controlled stage (Warner Instruments QE-1) and lowered slowly below the melting temperature, stopping to take both a wide field fluorescence image of the bilayer and high-speed movies of the bound particles. The temperature never fluctuated more than $0.2\text{ }^{\circ}\text{C}$ during imaging. Movies at each temperature across multiple compositions were analyzed and an average MSD was extracted that subsequently provided the complex shear modulus as described earlier.

Viscoelasticity

Freestanding lipid bilayers, away from the melting temperature, exhibit viscoelastic behavior across a broad range of frequencies (DMPC/DOPC sample

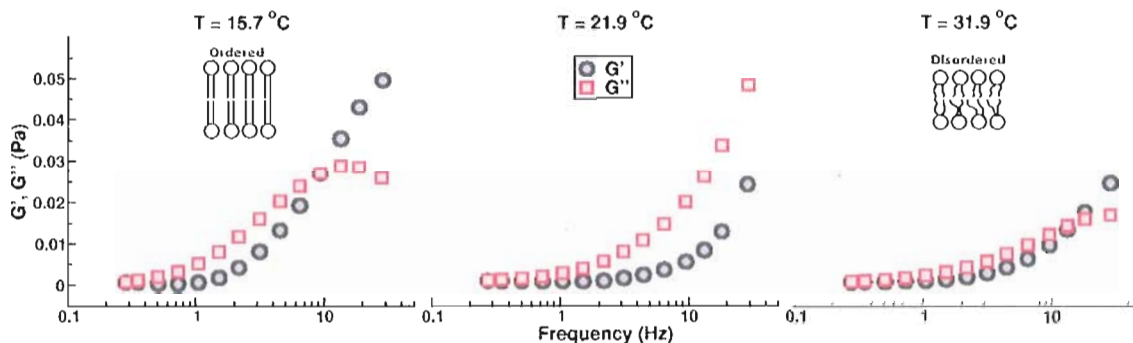


Figure 4.5: Representative DMPC/DOPC complex shear moduli. (*Left*) viscoelastic behavior in the liquid-ordered phase. (*Middle*) purely viscous behavior at the melting transition temperature. (*Right*) viscoelastic behavior in the liquid-disordered phase. The liquid-disordered phase exhibits a lower elastic response overall when compared to the liquid-ordered phase yet displays the same viscoelasticity.

shown in Figure 4.5). For ω above a crossover frequency the storage modulus dominates ($G' > G''$) while for ω below the crossover frequency the loss modulus dominates ($G'' > G'$). Our observations form the first demonstration of viscoelasticity in lipid membranes.

Membrane viscoelasticity is temperature dependent, surprisingly, becoming purely viscous at the melting transition temperature. The shape of the complex shear modulus is reminiscent of the Maxwell Model presented earlier. Moduli are well fit by Equation 4.4 and crossover frequencies can be extracted from these fits even if the crossover is slightly outside of the previously determined 0.1 to 33Hz window. Viscoelasticity is present in all systems examined: DMPC/DOPC, DMPS/DOPC, DMPC, DLPA, and DNPC membranes.

Temperature Sensitivity

Plotting the crossover frequencies as a function of the reduced temperature ($T - T_M$) reveals divergent behavior around the melting temperature (Figure 4.6). The viscoelasticity exhibited by pure lipid bilayers is striking not only in its persistence across multiple compositions, but also in its sensitivity to the liquid-ordered to liquid-disordered phase transition of the bilayers. This behavior occurs in lipids with both saturated (DNPC) and unsaturated (DMPC, DMPS, DLPA) tailgroups. Lipids with unsaturated, short tailgroups (DLPA) show a higher mean crossover frequency away from the transition temperature compared to unsaturated, long tailgroup lipids (DMPC and DMPS). This difference may be an indication of the increased fluidity of short chain lipids as the viscous modulus dominates more of the frequency bandwidth. All three DM lipids have similar mean crossover frequencies away from the transition temperature. This observation, together with the similar behavior of all five lipid samples with varying headgroups and the dependence of the melting transition on lipid tailgroups implies viscoelasticity is primarily determined by interactions between tailgroups.

Discovering the root of viscoelastic behavior may go hand in hand with elucidating the nature of the lipid melting transition. It has been suggested that the melting transition is first order [119–121] but there is little evidence to support the assertion. Our data provide support for higher a order melting transition. The divergence of the crossover frequency near the transition temperature is indicative of a second order

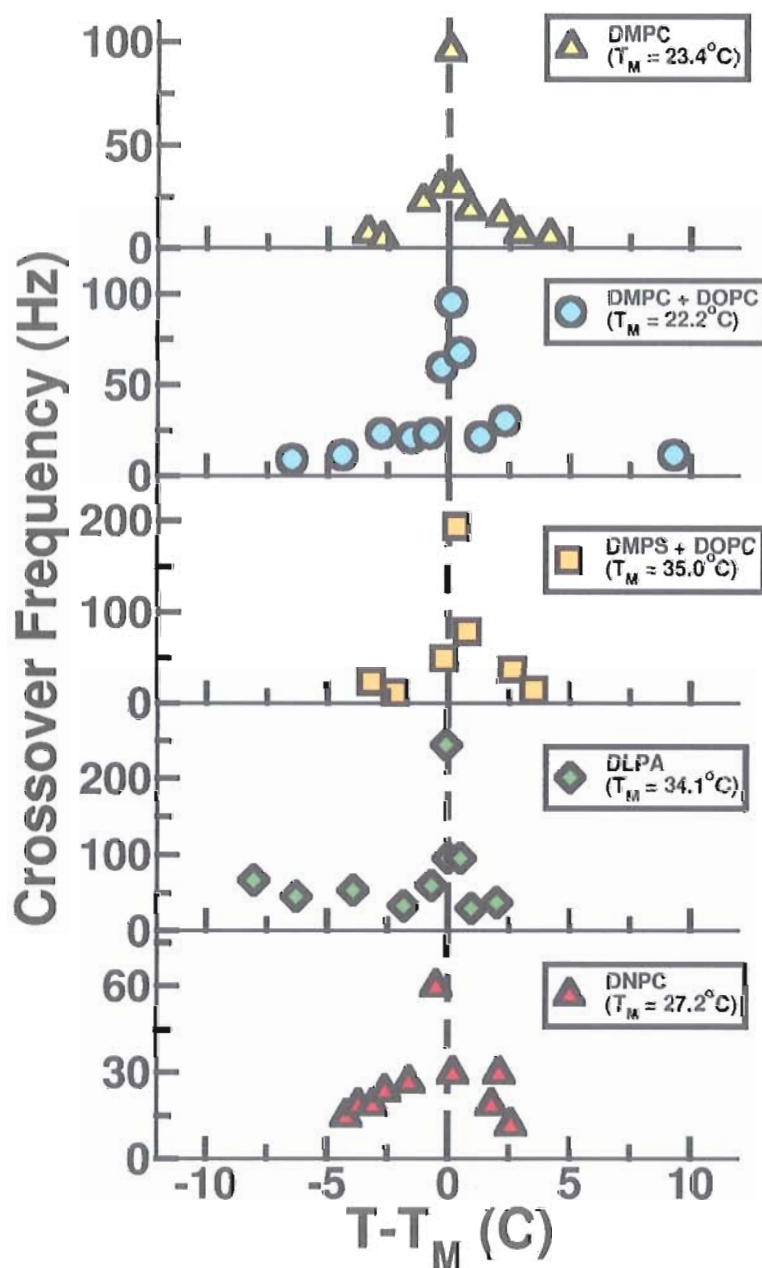


Figure 4.6: Combined plot of crossover frequencies for freestanding lipid bilayer samples as a function of reduced temperature. Despite the compositional differences between the samples, including the structural differences of the majority components, all samples show a similar divergent behavior at the crossover frequency. Mean crossover frequency away from the transition temperature is tailgroup dependent with shorter tailgroups (DL) producing high frequencies while longer tailgroups display lower frequencies (DM).

transition since a first order transition would provide no such evidence of a transition point. If the transition were first order we would experience small domain fluctuations near the critical temperature resulting in regions of liquid-ordered phase in a sea of liquid-disordered and vice versa.

Summary and Outlook

The viscoelasticity measured here constitutes the first observation of such behavior in lipid bilayers. The implications of such characterization extend to nearly all lipid membrane work. The extent to which lipid bilayer viscoelasticity influences inter-membrane and membrane associated proteins remains unexplored. If such proteins undergo conformational changes or perturbations at frequencies near the lipid crossover frequency, the fluid response they experience may be complicated. The diffusion and conformational change of membrane proteins is often assumed to occur within an entirely viscous membrane fluid [85, 86, 88]. However, if the proteins diffuse quickly or undergo rapid conformational changes they may experience an elastic membrane response. Indeed there is some evidence that a purely viscous treatment of protein diffusion in membranes is not accurate [87, 89, 122].

The results presented here provide directions for future work: the elucidation of the molecular basis of viscoelasticity and characterization of the effect of viscoelasticity on membrane associated proteins. A combination of experiment, theory, and simulation may make significant strides in finding the molecular lipid components responsible for

the observed viscoelasticity. Pairing these lines of inquiry may allow for the simulation of first- or second-order phase transitions in lipid bilayers that take into consideration viscoelasticity. Subsequent comparisons of these simulations to data presented in this work may help assign behavior to molecular components. Characterization of membrane proteins can proceed more directly from the work presented here given that many important proteins could readily incorporate into our freestanding lipid bilayer system. Using the microrheological measurements similar to ours in combination with spectroscopic or other protein conformation techniques may find correlations between protein behavior and membrane fluid properties.

Two-Point Microrheology

The system presented here can be improved significantly by the incorporation of two-point microrheology measurements [116, 117, 123–127]. Two-point microrheology measures correlations between pairs of particles rather than the single particle trajectories utilized in this work (Figure 4.7). By using correlations, the effect of the particle linker on measured properties is eliminated. In a two-point measurement, a correlation tensor is constructed as follows [128]:

$$D_{\alpha\alpha}(r, \tau) = \langle \Delta r_{\alpha}^i(t, \tau) \Delta r_{\alpha}^j(t, \tau) \delta(r - R^{ij}(t)) \rangle_{i \neq j, t} \quad (4.6)$$

where α denotes the correlation direction, i and j label the particles, R is the particle pair separation, Δr is the particle step vector, τ is the time needed to take that step, and the brackets indicate an average over all pairs. In practice, the diagonal elements of this tensor are of general interest: $D_{rr}(R, \tau)$ and $D_{\theta\theta}(R, \tau)$ the parallel

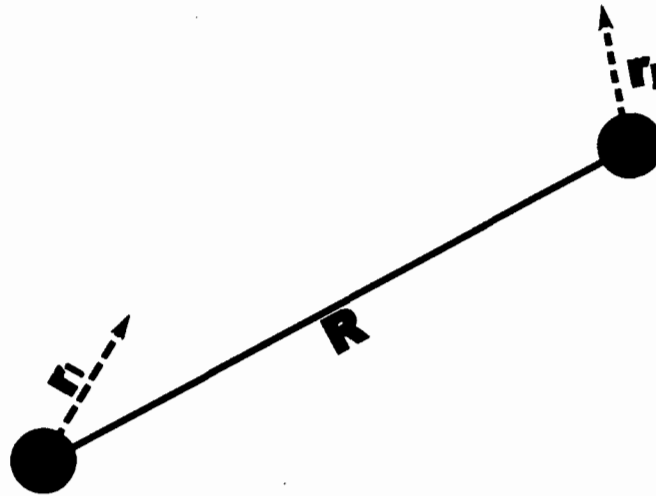


Figure 4.7: Illustration of the important vectors in two-point microrheology that measure the correlations between the Brownian motion of particle pairs.

and perpendicular correlations, respectively. These correlations, in the case of purely viscous fluids, are related to the fluid viscosity [86].

A technical hurdle that must be overcome to implement two-point microrheology is related to that amount of data needed to correctly extract correlations from Brownian dynamics. Two-point measurements look for similarities in tracer step vectors and detecting these above the background of random thermal motion requires large data sets. Our initial attempts to use two-point microrheology were cut short by the noise in our data. To better characterize the minimum amount of data needed we simulated correlated Brownian motion of tracer particles. In brief, $N = 50$ particles were randomly distributed on a two-dimensional plane. Every time step, a random particle was chosen and given a random thermal kick. Every other particle in the system was then given either a random thermal kick (not correlated) or moved along the same

vector as the initially chosen particle (i.e. perfectly correlated). The correlation was decided by comparing a random number to a correlation probability ($P(r)$) that was an inverse function of the distance from the chosen particle to the current particle ($P(0) = 1$ and $P(r) \propto 1/r$). We expect two-point microrheology to measure the inverse correlation as $D_{rr}(R) \propto 1/R$ [86]. Running this simulation as a series of total frames (or equivalently total times) from 100 to 10,000 provides a picture of the sensitivity of two-point microrheology on data density (Figure 4.8).

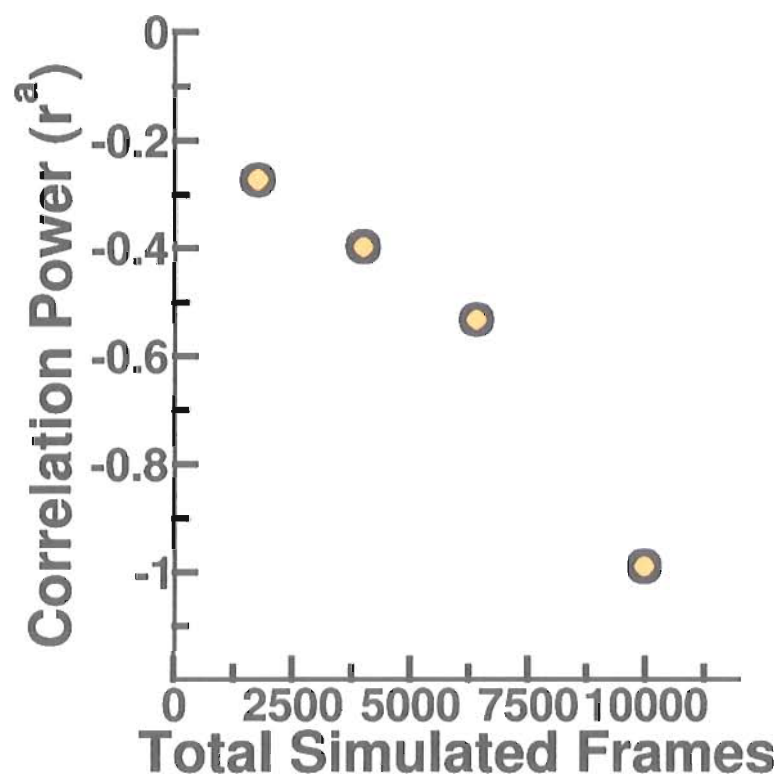


Figure 4.8: Plot of the falloff power of separation distance as a function of total number of frames in simulated two-point data. The simulation created an inverse separation dependence that should manifest as a power of -1. Only after the simulation of 50 particles at 1 frame per time step for 10,000 frames do we reach the correct result.

Simulating 50 particles at 1 frame per time step for 10,000 frames correctly recovers the inverse correlation. There appears to be structure in Figure 4.8 that may allow for less dense sampling by simply applying a correction to the measured values based on simulations but that assumes one knows the form of the true correlation. The simulation provides a minimum data density but not a restriction on how to reach the density. It may be possible to take pictures slowly for long periods of time or quickly for short periods of time and achieve the same result. Two-point microrheology is a powerful tool that, if applied to the membrane systems presented in this work, may elucidate properties of membrane fluidity not experimentally accessible previously. Moreover, there may be systems in which two-point measurements provide information not attainable with the one-point methods utilized in this work. An example of such a system is three component freestanding bilayers that undergo phase separation. Differences in the material properties of each phase may not be measurable with one-point methods given their dependence on the link between tracer and medium. Theoretical correlation functions for two-dimensional, purely viscous fluids have only recently been derived [86]. The work presented here motivates future theoretical work on viscoelastic, two-dimensional fluids as well as experiments that will guide and constrain theory.

APPENDIX

PERCOLATION SIMULATION

Site percolation simulations were written in MATLAB. Lattice-spanning probabilities $Q(p)$, where p is the site occupation probability, were generated by the simulated growth of percolation clusters on a 100×100 two-dimensional triangular lattice, see Figure A.1, by implementing the recursive Leath algorithm [129]. The algorithm performs the following recursive procedure: Each lattice site has three states including "occupied", "unoccupied", or "unexamined." All sites are initialized to unexamined with the exception of one designated occupied site. Starting at this occupied site, the size nearest neighbor sites are all examined and identified as either unoccupied, probability $(1 - p)$, or occupied, with probability p . When a nearest neighbor is identified as occupied, the program then repeats the examination process of this new site's nearest neighbors and so forth. With the recursive iteration of this procedure, the growth of a percolation cluster of occupied sites proceeds and can either stop, when all nearest neighbors are unoccupied, or continues until the cluster of occupied sites spans the distance from initial site to the lattice boundary. To build robust statistics of percolation we ran the simulation 1000 times for each value of p to determine the probability of a spanning cluster Q . To confirm our site percolation

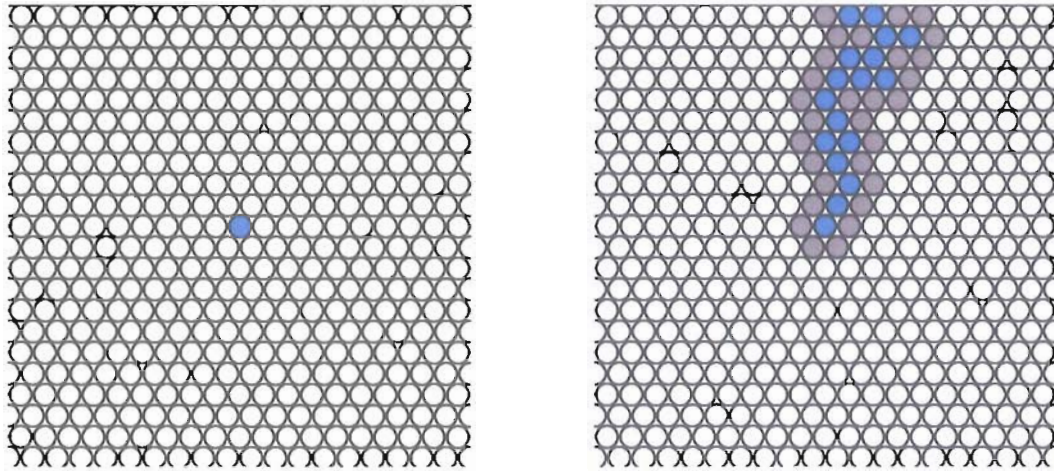


Figure A.1: Schematic drawings of a simulated triangular site percolation lattice. (*Left*) simulation lattice shown with all sites unexplored (white) except for an initial occupied point in the center (blue). (*Right*) representative spanning path of occupied sites (blue) surrounded by unoccupied sites (gray). The path is determined by a recursive, random, nearest neighbor search from the initial occupied point.

returns sane results, we compared our $Q(p)$ for $p_c = 0.5$ to the known analytic solution to which it matched well.

BIBLIOGRAPHY

- [1] B. Alberts, J. H. Wilson, and T. Hunt, *Molecular Biology of the Cell*, 5th ed. (Garland Science, New York, 2008).
- [2] H. F. Lodish, *Molecular Cell Biology*, 6th ed. (W.H. Freeman, New York, 2008).
- [3] R. Phillips, J. Kondev, and J. Theriot, *Physical Biology of the Cell* (Garland Science, New York, 2009).
- [4] V. von Tscharner and H. McConnell, *Biophysical Journal*, **36**, 421 (1981).
- [5] G. Barnes and I. Gentle, *Interfacial Science* (Oxford University Press, 2005).
- [6] R. Maoz and J. Sagiv, *Journal of Colloid and Interface Science*, **100**, 465 (1984).
- [7] G. Barnes and I. Gentle, *Interfacial Science* (Oxford University Press, 2005).
- [8] V. von Tscharner and H. M. McConnell, *Biophysical Journal*, **36**, 421 (1981).
- [9] R. Merkel, E. Sackmann, and E. Evans, *Journal de Physique*, **50** (1989).
- [10] M. Hetzer, S. Heinz, S. Grage, and T. M. Bayerl, *Langmuir*, **14**, 982 (1998).
- [11] E. Sackmann, *Science*, **271**, 43 (1996).
- [12] M. Winterhalter, *Current Opinion in Colloid and Interface Science*, **5**, 250 (2000).
- [13] P. Van Gelder, F. Dumas, and M. Winterhalter, *Biophysical Chemistry*, **85**, 153 (2000).
- [14] R. Fettiplace and D. Haydon, *Physiological Reviews*, **60**, 510 (1980).
- [15] L. Bagatolli, *Chemistry and Physics of Lipids*, **122**, 137 (2003).
- [16] L. Bagatolli and E. Gratton, *Biophysical Journal*, **79**, 434 (2000).

- [17] A. Sonnleitner, G. Schutz, and T. Schmidt, *Biophysical Journal*, **77**, 2638 (1999).
- [18] A. Ulman, *Chemical Reviews*, **96**, 1533 (1996).
- [19] M. Porter, T. Bright, D. Allara, and C. Chidsey, *Journal of the American Chemical Society*, **109**, 3559 (1987).
- [20] M. Montal and P. Mueller, *Proceedings of the National Academy of Sciences*, **69**, 3561 (1972).
- [21] M. Collins and S. Keller, *Proceedings of the National Academy of Sciences*, **105**, 124 (2008).
- [22] P. Mueller, D. Rudin, H. Tien, and W. Wescott, *The Journal of Physical Chemistry*, **67**, 534 (1963).
- [23] E. Barany-Wallje, S. Keller, S. Serowy, S. Geibel, P. Pohl, M. Bienert, and M. Dathe, *Biophysical Journal*, **89**, 2513 (2005).
- [24] S. Keller, S. Bezrukov, S. Gruner, M. Tate, I. Vodyanoy, and V. Parsegian, *Biophysical Journal*, **65**, 23 (1993).
- [25] H. He, Y. Cai, M. Sun, and H. Corke, *Journal Agricultural and Food Chemistry*, **50**, 368 (2002).
- [26] P. Bondioli, C. Mariani, A. Lanzani, E. Fedeli, and A. Muller, *Journal of the American Oil Chemists' Society*, **70**, 763 (1993).
- [27] O. Catchpole, J. von Kamp, and J. Grey, *Industrial and Engineering Chemistry Research*, **36**, 4318 (1997).
- [28] R. Parthasarathy and J. Groves, *Cell Biochemistry and Biophysics*, **41**, 391 (2004).
- [29] R. Brown, *The Philosophical Magazine*, **4**, 161 (1828).
- [30] A. Einstein, *Investigations on the Theory of the Brownian Movement*, edited by R. Fürth (Dover, New York, 1956).
- [31] H. C. Berg, *Random Walks in Biology* (Princeton University Press, Princeton, NJ, 1993).
- [32] T. Meyvis, S. D. Smedt, P. V. Oostveldt, and J. Demeester, *Pharmaceutical Research*, **16**, 1153 (1999).

- [33] C. W. Harland, D. Rabuka, C. R. Bertozzi, and R. Parthasarathy, *Biophysical Journal*, **94**, 4718 (2008).
- [34] E. Hecht and A. Zajac, *Optics*, 3rd ed. (Addison Wesley, Reading, Mass., 1997).
- [35] J. Crocker and D. Grier, *Journal of Colloid and Interface Science*, **179**, 298 (1996).
- [36] C. Dye, S. Scheele, P. Dolin, V. Pathania, M. Raviglione, *et al.*, *Journal of the American Medical Association*, **282**, 677 (1999).
- [37] E. L. Corbett, C. J. Watt, N. Walker, D. Maher, B. G. Williams, M. C. Raviglione, and C. Dye, *Archives of Internal Medicine*, **163**, 1009 (2003).
- [38] W. H. Organization, *Global Tuberculosis Control: Surveillance, Planning, Financing. WHO Report*, Tech. Rep. (World Health Organization, Geneva, 2007).
- [39] W. A. Volk, D. C. Benjamin, R. J. Kadner, and J. T. Parsons, *Essentials of Medical Microbiology*, Vol. 3rd ed. (J. B. Lipincott Co., Philadelphia, PA, 1986).
- [40] K. Desikan *et al.*, *Leprosy Review*, **66**, 287 (1995).
- [41] A. Fraise, P. A. Lambert, and J. Maillard, *Russell, Hugo & Ayliffe's Principles and Practice of Disinfection, Preservation & Sterilization*, Vol. 4th (Wiley-Blackwell, New York, 2004).
- [42] C. R. Smith, *American Review of Tuberculosis*, **45**, 334 (1942).
- [43] D. C. Twitchell, *Transactions of the National Association for the Study and Prevention of Tuberculosis*, Annual Meeting, 221 (1905).
- [44] M. Soparkar, *Indian Journal of Medical Research*, **4**, 627 (1917).
- [45] J. V. der Hoeden, *Zoonoses* (Elsevier, New York, 1964).
- [46] C. Barry, R. Lee, K. Mdluli, A. Sampson, B. Schroeder, R. Slayden, and Y. Yuan, *Progress in Lipid Research*, **37**, 143 (1998).
- [47] J. Asselineau, *The Bacterial Lipids* (Holden-Day Inc., San Francisco, CA, 1966).
- [48] P. Brennan and H. Nikaido, *Annual Review of Biochemistry*, **64**, 29 (1995).
- [49] D. E. Minnikin, in *The Biology of the Mycobacteria*, edited by C. Ratledge and J. Stanford (1982).
- [50] R. Hunter, M. Olsen, C. Jagannath, and J. Actor, *American Journal of Pathology*, **168**, 1249 (2006).

- [51] M. Kai, Y. Fujita, Y. Maeda, N. Nakata, S. Izumi, I. Yano, and M. Makino, *FEBS letters*, **581**, 3345 (2007).
- [52] H. Noll and H. Bloch, *American Review of Tuberculosis*, **67**, 828 (1953).
- [53] H. Noll and H. Bloch, *Journal of Biological Chemistry*, **214**, 251 (1955).
- [54] A. Bekierkunst, I. S. Levij, E. Yarkoni, E. Vilkas, A. Adam, and E. Lederer, *Journal of Bacteriology*, **100**, 95 (1969).
- [55] J. Indrigo, R. Hunter Jr, and J. Actor, *Microbiology*, **149**, 2049 (2003).
- [56] R. Ryll, Y. Kumazawa, and I. Yano, *Microbiology and Immunology*, **45**, 801 (2001).
- [57] M. S. Glickman, J. S. Cox, and W. R. J. Jacobs, *Molecular Cell*, **5**, 717 (2000).
- [58] R. Hunter, M. Olsen, C. Jagannath, and J. Actor, *Annals of Clinical & Laboratory Science*, **36**, 371 (2006).
- [59] A. D. Elbein and M. Mitchell, *Journal of Bacteriology*, **113**, 863 (1973).
- [60] A. D. Elbein, Y. T. Pan, I. Pastuszak, and D. Carroll, *Glycobiology*, **13**, 17 (2003).
- [61] J. H. Crowe, F. A. Hoekstra, and L. M. Crowe, *Annual Reviews in Physiology*, **54**, 579 (1992).
- [62] J. Crowe, L. Crowe, and D. Chapman, *Science*, **223**, 701 (1984).
- [63] F. Albertorio, V. A. Chapa, X. Chen, A. J. Diaz, and P. S. Cremer, *Journal of the American Chemical Society*, **129**, 10567 (2007).
- [64] D. Minnikin, *The Biology of the Mycobacteria*, edited by C. Ratledge and J. Stanford (Academic Press: New York, 1982).
- [65] J. Liu, E. Y. Rosenberg, and H. Nikaido, *Proceedings of the National Academy of Sciences*, **92**, 11254 (1995).
- [66] J. Liu, H. E. Takiff, and H. Nikaido, *Journal of Bacteriology*, **178**, 3791 (1996).
- [67] B. Dmitriev, S. Ehlers, E. Rietschel, and P. Brennan, *International Journal of Medical Microbiology*, **290**, 251 (2000).
- [68] S. Costigan, P. Booth, and R. Templer, *Biochimica et Biophysica Acta (BBA) - Biomembranes*, **1468**, 41 (2000).
- [69] R. Almog and C. A. Mannella, *Biophysical Journal*, **71**, 3311 (1996).

- [70] G. Retzinger, S. Meredith, K. Takayama, R. Hunter, and F. Kezdy, *Journal of Biological Chemistry*, **256**, 8208 (1981).
- [71] L. M. Crowe, B. J. Spargo, T. IONEDA, B. L. Beaman, and J. H. Crowe, *Biochimica et Biophysica Acta (BBA) - Biomembranes*, **1194**, 53 (1994).
- [72] M. Holden, S. Jung, T. Yang, E. Castellana, and P. Cremer, *Journal of the American Chemical Society*, **126**, 6512 (2004).
- [73] V. Torchilin, *Critical Reviews in Therapeutic Drug Carrier Systems*, **2**, 65 (1985).
- [74] V. Torchilin, *Cellular and molecular life sciences*, **61**, 2549 (2004).
- [75] C. W. Harland, Z. Botyanszki, D. Rabuka, C. R. Bertozzi, and R. Parthasarathy, *Langmuir*, **25**, 5193 (2009), ISSN 0743-7463.
- [76] J. Chen, Y. Kimura, and S. Adachi, *LWT-Food Science and Technology*, **40**, 412 (2007).
- [77] M. Edidin, *Annual Review of Biophysics and Bioengineering*, **3**, 179 (1974).
- [78] M. M. Poo and R. A. Cone, *Nature*, **247**, 438 (1974).
- [79] P. G. Saffman and M. Delbrück, *Proceedings of the National Academy of Sciences*, **72**, 3111 (1975).
- [80] M. Edidin, Y. Zagayansky, and T. J. Lardner, *Science*, **191**, 466 (1976).
- [81] R. Peters and K. Beck, *Proceedings of the National Academy of Sciences*, **80**, 7183 (1983).
- [82] W. Vaz, F. Goodsaid-Zalduondo, and K. Jacobson, *FEBS letters*, **174**, 199 (1984).
- [83] K. Jacobson, A. Ishihara, and R. Inman, *Annual Review of Physiology*, **49**, 163 (1987).
- [84] A. R. Dibble, A. K. Hinderliter, J. J. Sando, and R. L. Biltonen, *Biophysical Journal*, **71**, 1877 (1996).
- [85] M. A. Haidekker, T. Ling, M. Anglo, H. Y. Stevens, J. A. Frangos, and E. A. Theodorakis, *Chemistry and Biology*, **8**, 123 (2001).
- [86] A. J. Levine and F. C. MacKintosh, *Physical Review E*, **66**, 61606 (2002).

- [87] Y. Gambin, R. Lopez-Esparza, M. Reffay, E. Sieracki, N. Gov, M. Genest, R. Hodges, and W. Urbach, *Proceedings of the National Academy of Sciences*, **103**, 2098 (2006).
- [88] G. Guigas and M. Weiss, *Biophysical Journal*, **91**, 2393 (2006).
- [89] A. Naji, A. J. Levine, and P. A. Pincus, *Biophysical Journal*, **93**, L49 (2007).
- [90] H. Scott, *Current Opinion in Structural Biology*, **12**, 495 (2002).
- [91] W. Ash, M. Zlomislic, E. Oloo, and D. Tieleman, *Biochimica et Biophysica Acta (BBA) - Biomembranes*, **1666**, 158 (2004), ISSN 00052736.
- [92] L. Forrest and M. Sansom, *Current Opinion in Structural Biology*, **10**, 174 (2000).
- [93] T. Heimburg, P. Hildebrandt, and D. Marsh, *Biochemistry*, **30**, 9084 (1991).
- [94] T. Heimburg and D. Marsh, *Biophysical Journal*, **65**, 2408 (1993).
- [95] T. Heimburg and R. L. Biltonen, *Biophysical Journal*, **70**, 84 (1996).
- [96] O. G. Mouritsen and K. Jorgensen, *Current Opinion in Structural Biology*, **7**, 518 (1997).
- [97] T. Heimburg, *Biochimica et Biophysica Acta (BBA) - Biomembranes*, **1415**, 147 (1998).
- [98] I. P. Sugár, T. E. Thompson, and R. L. Biltonen, *Biophysical Journal*, **76**, 2099 (1999).
- [99] J. Nagle, *Annual Review of Physical Chemistry*, **31**, 157 (1980).
- [100] D. Brown and E. London, *Journal of Membrane Biology*, **164**, 103 (1998).
- [101] W. Sun, R. Suter, M. Knewton, C. Worthington, S. Tristram-Nagle, R. Zhang, and J. Nagle, *Physical Review E*, **49**, 4665 (1994).
- [102] M. Edidin, *Nature Reviews Molecular Cell Biology*, **4**, 414 (2003).
- [103] O. Mouritsen and K. Jørgensen, *Chemistry and physics of lipids*, **73**, 3 (1994).
- [104] J. Nagle, *Faraday Discussions of the Chemical Society*, **81**, 151 (1986).
- [105] J. Nagle, *Journal of Membrane Biology*, **27**, 233 (1976).
- [106] L. Tamm and H. McConnell, *Biophysical Journal*, **47**, 105 (1985).

- [107] R. Koynova and M. Caffrey, *Biochimica et Biophysica Acta (BBA)-Reviews on Biomembranes*, **1376**, 91 (1998).
- [108] H. Ebel, P. Grabitz, and T. Heimburg, *Journal of Physical Chemistry B*, **105**, 7353 (2001).
- [109] H. Barnes, J. Hutton, and K. Walters, *An Introduction to Rheology* (Elsevier Science Ltd, 1989).
- [110] P. Cicuta and A. Donald, *Soft Matter*, **3**, 1449 (2007).
- [111] J. W. Goodwin and R. W. Hughes, *Rheology for Chemists: an Introduction*, 2nd ed. (RSC Publishing, Cambridge, UK, 2008).
- [112] T. G. Mason, *Rheologica Acta*, **39**, 371 (2000).
- [113] J. Weber, *Physical Review*, **101**, 1620 (1956).
- [114] K. M. van Vliet, *Physical Review*, **109**, 1021 (1958).
- [115] H. B. Callen, *Thermodynamics and an Introduction to Thermostatistics*, 2nd ed. (Wiley, 1985).
- [116] J. Crocker and B. Hoffman, *Methods in Cell Biology*, **83**, 142 (2007).
- [117] T. G. Mason, K. Ganesan, J. H. van Zanten, D. Wirtz, and S. C. Kuo, *Physical Review Letters*, **79**, 3282 (1997).
- [118] M. Caggioni, P. Spicer, D. Blair, S. Lindberg, and D. Weitz, *Journal of Rheology*, **51**, 851 (2007).
- [119] L. M. Loura, A. Fedorov, and M. Prieto, *Biophysical Journal*, **71**, 1823 (1996).
- [120] T. Gil, J. H. Ipsen, O. G. Mouritsen, M. C. Sabra, M. M. Sperotto, and M. J. Zuckermann, *Biochimica et Biophysica Acta (BBA)-Reviews on Biomembranes*, **1376**, 245 (1998).
- [121] M. Fidorra, T. Heimburg, and H. M. Seeger, Los Alamos National Laboratory, Preprint Archive, Physics, 1 (2007).
- [122] W. Vaz and H. Dieter, *FEBS Letters*, **152**, 287 (1983).
- [123] T. Waigh, *Reports on Progress in Physics*, **68**, 685 (2005).
- [124] D. Weihs, T. Mason, and M. Teitell, *Biophysical Journal*, **91**, 4296 (2006).
- [125] T. G. Mason and D. A. Weitz, *Physical Review Letters*, **74**, 1250 (1995).

- [126] S. Rogers, T. Waigh, and J. Lu, *Biophysical journal*, **94**, 3313 (2008).
- [127] A. Mukhopadhyay and S. Granick, *Current Opinion in Colloid and Interface Science*, **6**, 423 (2001).
- [128] V. Prasad, S. Koehler, and E. Weeks, *Physical Review Letters*, **97**, 176001 (2006).
- [129] P. Leath, *Physical Review B*, **14**, 5046 (1976).